Ph.D. Dissertation

DEVELOPMENT OF A SIMULATION ENVIRONMENT FOR THE ANALYSIS AND THE OPTIMAL DESIGN OF FLUORESCENCE DETECTORS BASED ON SINGLE PHOTON AVALANCHE DIODES

Marina Repich

Advisor:
Prof. Gian-Franco Dalla Betta
Università degli Studi di Trento
Co-Advisor:
Dr. David Stoppa
Fondazione Bruno Kessler

ICT International Doctoral School
DISI - The University of Trento
April 2010

To my fiancé for his love,
support and understanding

Abstract

Time-resolved fluorescence measurements enable the study of structure of molecular systems and dynamical processes inside them. This is possible because of a very high sensitivity of fluorescence lifetime to the physical and chemical properties of micro-environment in which fluorophores are situated. However, proper detection of the fluorescence lifetime is a challenging task, due to the fact that the fluorescence decay time of commonly used fluorophores lies in a nanosecond range. This puts strict requirements on the parameters of the fluorescence detectors.

The features of single-photon avalanche diodes (SPAD) make these optical detectors a good alternative to conventional photomultiplier tubes and micro-channel plates. CMOS technology allows cointegration of a SPAD and electronic circuits on the same substrate and provides advantages in time resolution and noise characteristics. Monolithic integration of signal processing circuits and detectors on the same chip allows using such detectors without additional external hardware.

New SPAD sensors with improved characteristics are produced every year. However, the designers consider various performance metrics while the importance of each particular detector characteristic depends on its application. Therefore, the validation and optimization of SPAD characteristics should be performed in a close connection with the analysis of a specific system, wherein this detector will be used.

This work was aimed at developing of a model able to describe a typical *fluorescence experiment with SPAD-based detector. The model simulates all essential parts of the fluorescence experiment starting from the light emission, through photo-physical processes occurring inside a bio-sample, to a detector itself and read-out electronics.*

The ability of the developed model to simulate various light sources (laser and micro-LED), fluorescence measurement techniques (time-correlated single photon counting and time-gating) was verified. The simulated results were in good agreement with the experimental data and the model proved its flexibility. Furthermore, the model provided the explanation of the distortions in experimental fluorescent curves measured under a very high ambient light when pile-up effects appear. Finally, a set of virtual experiments were established to investigate the influence of noisy pixels in SPAD array on a lifetime estimation and to study the feasibility of time-filtering instead of conventional optical filtering. Simulation results are in good agreement with data available in literature.

Keywords [single photon avalanche diode, fluorescence decay, simulation modelling, time-correlated single photon counting, time-gating]

Acknowledgements

First of all, I would like to thank my advisors David Stoppa and Gian–Franco Dalla Betta, whos motivation, pedagogic skills, patience with my English and constant attention allowed me to start and to complete this project.

I also want to thank my first advisors Vladimir Apanasovich, Vladimir Lutkovski and Mikalai Yatskou (Belarusian State University) for the initial understanding of what research is.

Many thanks to Robert K. Henderson (The University of Edinburgh) and people from his group: Bruce R. Rae, Keith R. Muir, Justin A. Richardson, Richard J. Walker, Day-Uei Li, Alex Buts and David Tyndall, for the acquaintance with Scottish science and those remarkable winter and summer schools. In particular, I would like to thank Bruce and Sabrina for supporting me not only during the internship in Scotland but also when I was writing this thesis; David and Lisa for the wonderful trip through the Northern Ireland; Justin for lessons about Scottish history; Keith for friendly chats about everything. Special thanks to David Renshaw for the help with MATLAB code optimization and his warm attitude to me. It was a great pleasure to spend those 6 months at Edinburgh!

Thanks to Petr Nazarov, Sergey Laptenok and Aleh Kavalenka, who set an example of a successful Ph.D. to me. I am particularly grateful to Petr for leading me to a scientific track and for our discussions about biology and statistical analysis.

My warm appreciation to my mother, brother and sister for their eternal faith in me. They always admired my achievements no matter how significant those were.

Ida Sri Rejeki Siahaan, it was great to be your roommate and a friend. I will never forget our long conversations about culture of our countries, sari evening and many other things. Best wishes for your life and career! Terima kasih!

Special thanks to my good friends Ruslan Asaula, Leshka Chayka, Artem Evtiukhin, Sasha Autayeu, Lena Simalatsar, for our eventful life outside research. Thanks to all the boys and girls from the Russian-speaking community of the University of Trento for the time spent together. Sasha, Olya, Tanya, Vovka, Natasha, Kolya, Andrey, Anton, Vitya, another Sasha, Lena, another Kolya, Yura, Sergey, Vanya, Maks, Egor, as well as all the others — our pelmeni parties, public birthdays and self-organizing trips were an integral part of these years.

Finally, I would like to thank my future husband Andrei. Writing this thesis without him would have been a million times harder.

Abbreviations

CCD	Charge-Coupled Device
CMOS	Complementary Metal Oxide Semiconductor
DCR	Dark Count Rate
FIDA	Fluorescence Intensity Distribution Analysis
FRET	Förster Resonance Energy Transfer
FWHM	Full Width at Half Maximum
GUI	Graphical User Interface
LED	Light-Emitting Diode
MCP	Micro-Channel Plate
OW	Observation Window
PDF	Probability Density Function
PDP	Photon Detection Probability
PMT	Photomultiplier Tube
QY	Quantum Yield
RAM	Random Access Memory
SPAD	Single Photon Avalanche Diode
TCSPC	Time-Correlated Single Photon Counting

Contents

List of Tables

List of Figures

Publications

- Marina Repich, David Stoppa, Gian-Franco Dalla Betta, "Simulation modelling of a micro-system for time-resolved fluorescence measurements," Accepted for publication in Proceedings of SPIE 7726, Belgium, April 2010.

- Marina Repich, David Stoppa, Gian-Franco Dalla Betta, "Analysis of time filtering of excitation light in fluorescence measurement with simulation modelling," Accepted for publication in Proceedings of IT-EDS2010, Belarus, April 2010.

- Marina Repich, David Stoppa, Lucio Pancheri, Gian-Franco Dalla Betta, "Simulation modelling for the analysis and the optimal design of SPAD detectors for time-resolved fluorescence measurements," Proceedings of SPIE 7355, pp. 73550O, Czech Republic, April 2009.

Chapter 1

Introduction

1.1 The Context

Fluorescence lifetime detection is a well-known and widely used method of study of biological objects. This is due to the fact that the excited state lifetime is highly sensitive to the fluorophore's chemical environment. For example, an increase of porphyrin markers fluorescence lifetime (in comparison to the control cells) allows detection of tumours at very early stages [1]; also, fluorescence allows measurement of oxygen concentration inside cells since oxygen is a quencher of the fluorescence [2]. In general, time-resolved fluoresce provides information about the size and the shapfjhngdfge of molecules and dynamic processes that happen in the solution in a nanosecond scale. Also the Förster resonance energy transfer (FRET) technique, as a part of fluorescence lifetime detection, can be used to determine the structure of complex molecules, such as proteins [3].

The typical equipment for fluorescence lifetime measurement includes a narrow-wavelength light source to excite the selected fluorophore, an optical system to separate the excitation and fluorescent light and a high-sensitivity photodetector. Due to some limitations in the performance of light sources, the frequency-domain measurements were historically the first ones. In 1921, Wood [4] measured small phase changes to determine the time interval between the absorption and emission of light. About 40 years later, the time-domain measurements became possible due to the flashlamps serving as excitation sources [5]. With the appearance of subnanosecond pulsed light sources, the capabilities of the time-domain measurements have been increased. At the present time, the most popular excitation light source is a picosecond pulsed laser.

Major changes also occurred on the detector side. PhotoMultiplier Tubes (PMTs) were the first detectors used in fluorescence measurements. They provide low noise and fairly high quantum detection efficiency in the visible range of radiation, but on the other hand they are bulky, fragile, expensive, require high supply voltage (2–3 kV) and are sensitive to electromagnetic fields and mechanical vibrations. All of this makes PMTs inapplicable for the construction of large arrays.

Solid-state single photon detectors became available much later. These devices, called "Single Photon Avalanche Diodes" (SPAD), operate biased above the breakdown voltage and generate macroscopic current pulses in response to the absorption of single photons. Since their operation principles are similar to those of Geiger counters, SPADs are also known as Geiger-mode Avalanche PhotoDiodes (GM-APDs). SPADs are an attractive alternative to PMTs due to the advantages of solid-state devices, such as: magnetic field immunity, robustness, long operative lifetime, small size, lower cost, lower operation voltage and suitability for building of integrated systems.

The progress in CMOS technology allows fabrication of the SPAD with additional advantages, such as low power consumption and high fabrication yield. This further decreases the cost and allows for the fabrication of monolithic arrays for large-area detection. Moreover, cointegration of SPADs and electronic circuits on the same substrate provides advantages in terms of time and noise characteristics. In addition, the on-chip implementation of the signal processing allows the use of such detectors without additional external hardware.

1.2 The Problem

The area of SPAD-based detectors is developing constantly and quickly. Different techniques of SPAD fabrication result in devices with different characteristics. Current research focuses mainly on the improvement of particular characteristics using different performance metrics and without consideration of the system context or specific application requirements. This results in appearance of detectors with one perfect characteristic while the others are not that good. Moreover, the development of new SPADs is a time- and money-consuming process, yet their suitability to a specific experiment is hard to predict.

On the other hand, there exists a wide range of works in theoretical and simulation-based investigations of single parts and internal processes of SPAD. Usually, they consider the SPAD on its own, without any relation to the application area. The study of the characteristics of SPAD-based detectors from a system perspective, taking into account the whole experimental setup and measurement technique, is missing.

1.3 The Solution

To study the properties of SPAD-based detectors in the context of fluorescence lifetime measurement experiment, we build a model of a typical experimental setup, from light source to read-out electronics. While the model is particularly focused on SPAD-based detectors, there are no restrictions for the rest of the experimental equipment. The proposed model is flexible enough to simulate various light sources (for example, laser or

LED) and different measurement techniques (such as time-correlated single photon counting and time-gating). The flexibility of the system enables it to easily adapt to different experimental setups and thus to be successfully employed in the wide variety of SPAD application areas.

Finally, the model can be used to *predict* both qualitative and quantitative results for a given experimental setup. This allows the manufacturers and researchers to save the time and efforts required for natural experiments, and thereby facilitates the development of detector systems that demonstrate the optimal performance in their target application.

1.4 Aims

The aim of this project was to create a tool that will allow the performance analysis and optimization of a SPAD-based system. The tool should take into account the knowledge about the influence of each SPAD characteristic on the global performance of the detection system. To reach this goal, the following tasks have been defined:

- Develop the simulation model of a SPAD detector together with readout electronics.
- Develop the simulation model of biophysical processes of light propagation and spectral/time domain light transformation within a fluorescent sample.
- Integrate the described unit models into the general model of the system, with consideration of geometry setup and the used measurement technique.
- Analyse the influence of certain SPAD characteristics on the global quality of the measurement system. Determine the optimal trade-off between opposing characteristics.

1.5 Structure of the Thesis

Chapter 2 provides an overview of the fluorescence process and its characteristics. Different types of fluorescence measurement are reviewed, with a particular focus on time-resolved techniques, such as time-correlated single photon counting and time-gating. The chapter also explains the operation principles of single photon avalanche diodes and summarizes the state-of-the-art of SPAD-based detectors.

A survey of existing works in theoretical and simulation-based analysis of SPAD-based detector performance, the analytical and simulation models of some parts and internal processes of SPAD are presented in Chapter 3. Also, an overview of the simulation of some biological objects that were investigated by means of detection of fluorescence lifetime, is provided.

Simulation modelling as a tool for the analysis of complex systems is introduced in Chapter 4. There we provide a complete description of the proposed model of fluorescence measurement setup and of the simulation workflow. We also describe the methods used, the assumptions made and other details of the modelling.

The experimental validation of the system is presented in Chapter 5. The qualitative and quantitative ability of the proposed model and its flexibility are verified by the simulation of different light sources, measurement techniques and experimental setups. The chapter also presents the results of the analysis of time-filtering efficiency and influence of noisy pixels in SPAD array on lifetime estimation for fluorescence-based bioaffinity assays.

Chapter 6 concludes the work and proposes a number of improvements of the model that might further increase the accuracy of the simulation and enable the consideration of more complex systems.

Chapter 2

Fluorescence experiment and SPAD detectors

This chapter provides an overview of the fluorescence process and its characteristics. Different types of fluorescence measurement are reviewed, with the main focus on time-resolved techniques, such as time-correlated single photon counting and time-gating. The operation principles of single photon avalanche diodes are described and some state-of-the-art SPAD-based detectors are presented.

2.1 Fluorescence

Fluorescence is a process of light emission by a substance that has absorbed light of a different wavelength. The characteristics of the fluorescence are:

- absorption and emission spectra,
- lifetime of excited state,
- degree of polarization,
- fluorescent anisotropy,
- energy,
- quantum yield.

Due to the Stokes shift the maximum of fluorescence emission spectrum is shifted to long-wave region in comparison to the maximum of the absorption spectrum [6, p. 13]. The absorption and emission spectra in frequency scale usually conform to the mirror symmetry rule [7, Section 1.3.2] (see Figure 2.1).

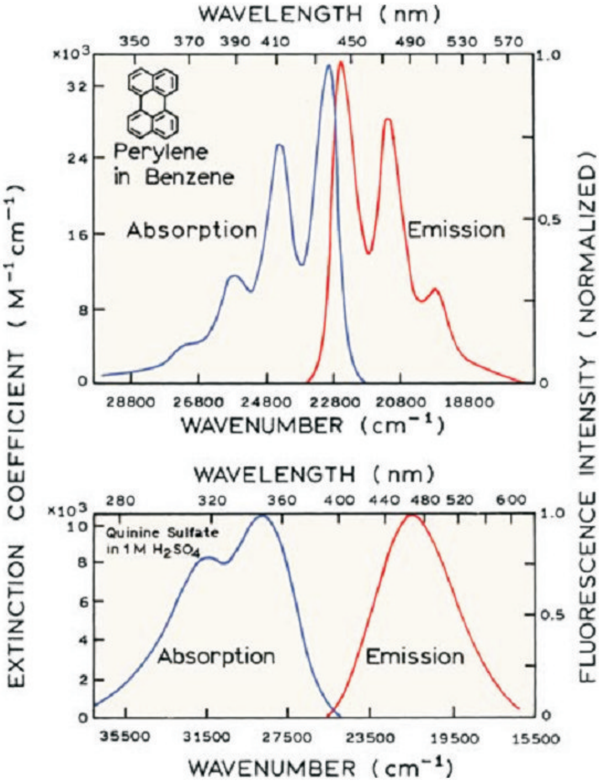

Figure 2.1: An example of the absorption and emission spectra [7, p. 4].

The absorption of light quantum by a fluorescent molecule transfers this molecule into an excited state as the result of electron transition to the higher energy level ($S_0 \to S_1$) (see Figure 2.2). This process takes $10^{-16} - 10^{-15}$ s. This time is not enough for the molecule nucleus to change its position and velocity (Franck–Condon principle) [8, Section 2.4]. This results in the growth of internal vibrational and potential energy. Further vibrational relaxation takes place in $10^{-12} - 10^{-11}$ s. The system comes

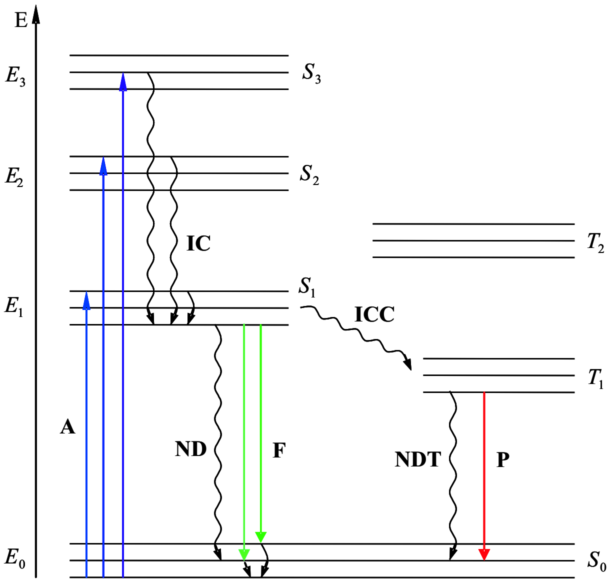

Figure 2.2: The Jablonski diagram. S_0 is the ground state; $S_1, S_2, ..., S_n$ is the system of singlet excited states; $T_1, T_2, ..., T_m$ is the system of triplet states. The processes are: A — absorption; IC — internal conversion; ICC — intercombination conversion; ND — nonradiative deactivation; F — fluorescence; NDT — nonradiative deactivation from triplet state; P — phosphorescence.

to the thermal equilibrium of the excited state. After a while occurs the transition to the ground state ($S_1 \rightarrow S_0$) with emission of a light quantum, i.e. fluorescence. The vibrational energy content under this transfer grows again with subsequent relaxation in $10^{-12} - 10^{-11}$ s.

The excited state (S_1) can be deactivated by different ways besides light emission. The possible options of excitation and deactivation are illustrated by the Jablonski diagram [7, Chapter 1] in Figure 2.2. An increase of the probability of nonradiative transitions leads to the quenching of fluorescence.

The lifetime of the excited state is determined by the total probability of the deactivation of this state

$$\tau = \frac{1}{k + r + \Gamma} , \tag{2.1}$$

where k is the rate constant of nonradiactive deactivation (ND transition in Figure 2.2, r is the rate constant of conversion into triplet states (ICC transition), Γ is the emission rate constant of the fluorophore (F transition). High values of the rate constants result in fluorescent lifetime of about $10^{-9} - 10^{-8}$ s.

The fluorescence quantum yield is defined as the ratio of the number of emitted photons to the number of photons absorbed by the system

$$QY = \frac{\Gamma}{\Gamma + k + r} \, . \tag{2.2}$$

The QY tends to unity when the sum of the rate constants of nonradiative deactivations $(k{+}r)$ tends to zero. The quantum yield of intrinsic (natural) fluorophores is around 0.1, while for special fluorescent probes the QY reaches 0.98. The energy yield is always less than unity because of the Stokes loss.

2.2 Time-resolved fluorescence detection

Fluorescence detection is a widely used technique due to its high time resolution and good sensitivity to composition changes of a sample. It is used in defectoscopy, microbiology, medicine, biophysics, etc. There are two main types of measurement of fluorescence lifetime: the frequency-domain and time-domain techniques.

2.2.1 Frequency-domain technique

In the frequency-domain technique, the fluorescent sample is excited by continuously modulated light. The fluorescence emission displays a phase shift and a modulation decrease (see Figure 2.3). The lifetimes can be determined as

$$\tau_\varphi = \frac{\tan(\varphi_{em} - \varphi_{ex})}{\omega} \, , \tag{2.3}$$

$$\tau_M = \frac{1}{\omega}\sqrt{\frac{1}{\left(\frac{M_{em}}{M_{ex}}\right)^2 - 1}}\,, \tag{2.4}$$

where τ_φ is the lifetime based on the phase shift, τ_M is the lifetime based on the modulation depth decrease, φ_{em}, φ_{ex} and M_{em}, M_{ex} are phase and modulation depth of the emitted and exciting lights, respectively; ω is the angular modulation frequency.

In the case of monoexponential decay τ_φ and τ_M are equal. In the case of multi-exponential decay $\tau_\varphi < \tau_M$ and the measurements should be repeated for multiple modulation frequencies [9, Section 2.3.1].

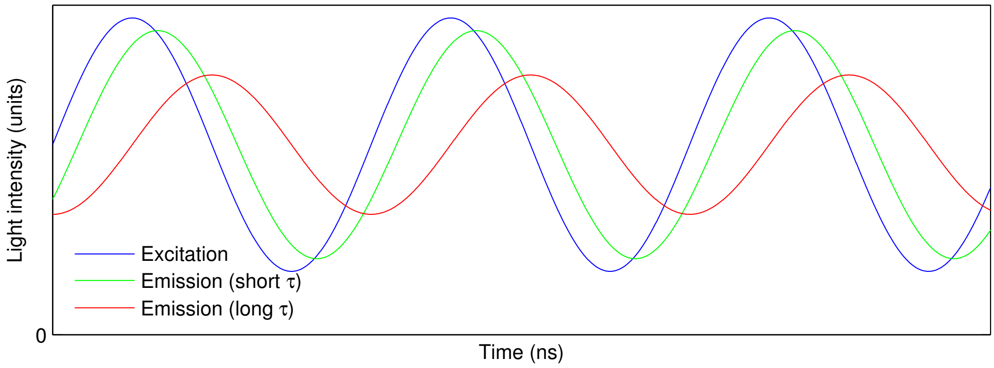

Figure 2.3: Frequency-domain lifetime measurement. The fluorescence emission demonstrates a phase shift and a modulation decrease in comparison with sinusoidally modulated excitation light.

2.2.2 Time-domain technique

In the time-domain, the fluorescence lifetime measurements can be done using two techniques: time-correlated single photon counting (TCSPC) and time-gating detection. In the former, the sample is excited by pulsed light source and the arrival time of the first fluorescent photon is recorded with a very high time resolution. The fluorescence decay curve is obtained by the detection of arrival time of a large number of photons. The light intensity is set to such a value that the probability to detect a photon per pulse is less than or equal to 1%, otherwise the intensity decay can be distorted to shorter times (pile-up effect) [7, Chapter 2].

In the case of monoexponential decay the fluorescence lifetime can be estimated as the slope of the fluorescence decay in logarithmic scale

$$I(t) = I_o \exp(-t/\tau) \quad \Rightarrow \quad \tau \text{ is the slope of } \log I(t) \text{ vs } t\,. \tag{2.5}$$

In the case of multi-exponential decay more complex methods should be used. For example, the lifetime in this case can be obtained using the following scheme. Firstly, the convolution of assumed fluorescence decay with a known instrumental response is calculated. Then the result is compared with the measured experimental decay curve using statistical fitting criterion, such as the chi-square test. The quality of the fit can be judged by the chi-square value and the autocorrelation of weighted residuals. The advantage of the described experimental technique is that the actual fluorescence decay is measured directly; the disadvantage is its relative slowness.

Time-gating

In the time-gating detection, the number of photons detected during two or more fixed time intervals are collected. For the measurement of a monoexponential fluorescence decay (see Figure 2.4), two time intervals with equal width are usually enough. The fluorescence lifetime τ in this case is calculated using

$$\tau = \frac{T_1 - T_2}{\ln(V_2/V_1)}\,, \tag{2.6}$$

where T_1 and T_2 are the time delays between the excitation pulse and the onset of the first and the second time intervals, respectively; V_1 and V_2 are the integrated intensities (i.e. number of counts) of these time intervals [10] (see Figure 2.4).

In the case of a multi-exponential fluorescence decay (which is the case for vast majority of biological samples) more time intervals and a correction of instrumental response are required. Therefore, the task of lifetime characterization becomes nontrivial.

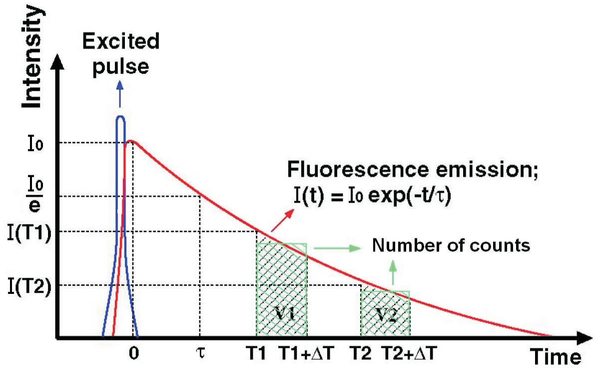

Figure 2.4: Mono-exponential fluorescence decay. Adapted from [11].

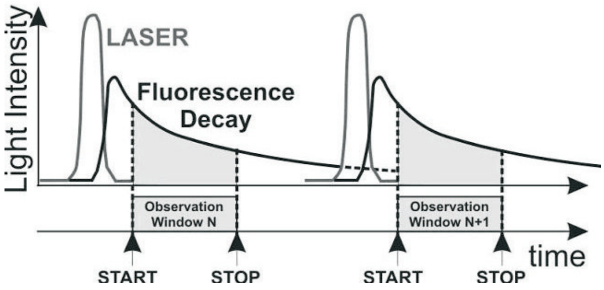

Figure 2.5: Modified time-gated measurement technique [12].

A slightly modified time-gated technique can be utilized in the SPAD detectors. The photons are collected during a nanosecond observation window (OW) synchronized with the light pulse (see Figure 2.5). The measurements are repeated the prescribed number of times to obtain a statistically significant result. The number of detected photons is allocated to a time slot. The observation window is then shifted by a picosecond time step and the measurement repeated from the start. Fluorescence decay convolved with the rectangular OW is prepared when the time range of interest has been fully scanned. The drawback of this schema, in comparison to the ordinary one, is demonstrated by photobleaching: the fluorophores are already bleached when the OW is shifted to the long time fluorescence tail, the detector counts only dark photons, and as a result the detected lifetime is shorter than the real one.

The integration of SPAD detectors into the CMOS process enables the manufacturers to embed the control and signal processing circuits into the same chip. This gives more flexibility in the selection of OWs' widths and positions. For example, the scheme with non-uniform observation windows is useful for increasing the efficiency of time-gating: longer OWs are used in the end of fluorescence decay (when the intensity is lower) to increase the collected number of counts.

Modern CMOS SPAD detectors use up to 4 observation windows [13] with width from 408 ps to 48 ns [14] and the accuracy in the positioning on time scale of 60 ps [15].

2.2.3 Typical fluorescence detection setup

A typical time-domain fluorometer is shown in Figure 2.6. The pulsed light goes through optical system and excites the fluorescence. The excitation source can be either a pulsed laser, a LED or a flash-lamp. This part of optical system can consist of a monochromator (narrow-band filter), an attenuator and a collecting lens. The electrical pulse associated with the optical pulse is generated and routed to the synchronization input of the data processing module. Meanwhile, the emitted fluorescence is collected at right angle with respect to the incident beam, and detected after passing through the optical system. This part of the optical system usually includes an excitation filter and a collecting lens. An MCP, PMT, CCD camera or SPAD can be used as a detector. Data processing depends on chosen technique (see Section 2.2.2).

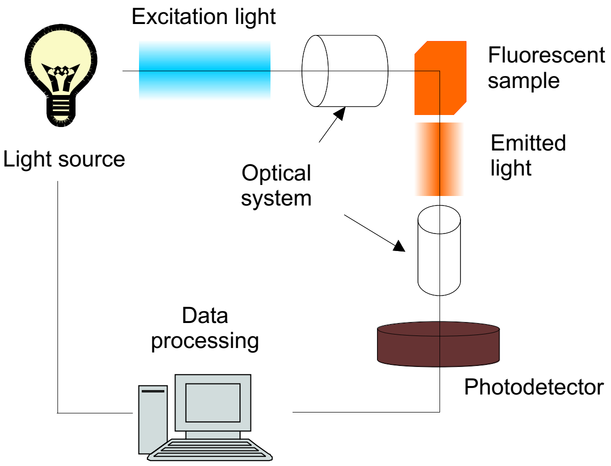

Figure 2.6: Typical time-domain fluorescence detection setup.

The photodetector determines the accuracy of the measurements. But the general performance is defined by all parts of the setup, from the light source to the lifetime extraction algorithm.

2.3 Single photon avalanche diode

Single-photon avalanche diodes (SPAD) are a class of semiconductor devices based on a p-n junction, reverse biased above breakdown voltage [16]. The electric field in the junction depletion region is so high that a single photon absorbed in this area can trigger a self-sustaining avalanche [17, 18].

The operation principle of an ideal SPAD is the following. In the quiescent state, when no current flows through the device and an excess bias voltage V_e is applied to the SPAD (see Figure 2.7), the electric field in the depletion region is high enough to create an avalanche caused by the smallest fluctuation. A single photon absorption in the depletion region results in the creation of an electron-hole pair that is immediately accelerated. This action results in a self-sustaining impact ionization avalanche

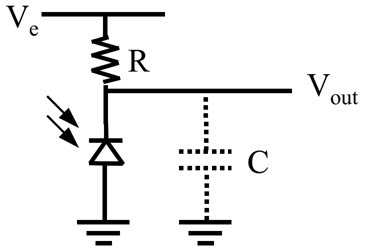

Figure 2.7: A simplified SPAD diagram.

process. The current immediately grows up to a constant level that is dependent on the excess bias voltage V_e and diode series resistance R. The external quenching circuit reduces the applied bias voltage, V_b, to a value lower than the breakdown voltage V_bd, which leads to the quenching of an avalanche. The operation cycle is completed by the reset of the excess bias voltage to its initial value. Thus, the output of the detector is a current pulse with a constant peak amplitude. The leading edge of this pulse indicates the time of photon arrival. The detector is insensitive to any photons arriving in the time between the start of the avalanche and the bias voltage being reset. This period is called the *dead time* of the SPAD.

Time resolution. Obviously, real SPADs differ from the ideal ones. The first characteristic of the imperfection is *time resolution*. Time resolution, or time jitter, is a statistical distribution of the delay between actual arrival time of the photon to the sensor and the leading edge of the output pulse. A typical SPAD time resolution curve has a fast peak followed by a slow exponential tail (see Figure 2.8).

The peak is due to the fact that the photons absorbed in the depletion region need different time to build up the avalanches. The full width at the half maximum (FWHM) of the peak is the time resolution of the detector. It can be improved by increasing the maximum electric field at the active junction, i.e. by increasing the excess bias voltage V_e. The tail is due to

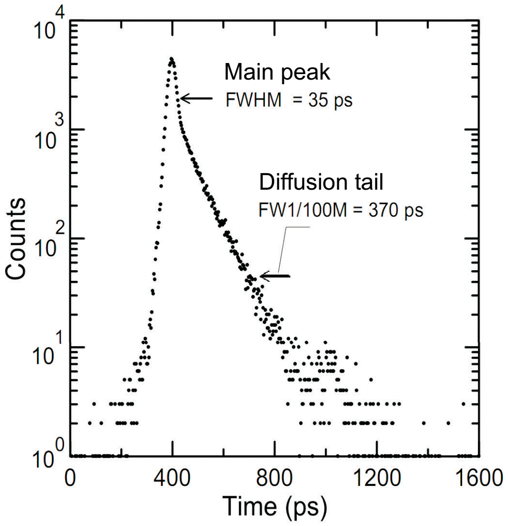

Figure 2.8: A typical time resolution curve of SPAD detector. The curve has a fast peak with FWHM=35 ps followed by a slow exponential tail with FWHM=80 ps. Adapted from [19].

the fact that minority carriers, which are created by the photons absorbed in neutral region, reach the depletion region by diffusion. Evidently, the diffusion tail depends on the photon wavelength. In some SPADs reported in the literature, the diffusion tail was greatly reduced by changing SPAD structures [20, 21].

Photon detection probability. The next characteristic of a real SPAD is the *photon detection probability* (PDP) which is defined as the ratio between the number of incoming photons and the number of the output current pulses. At the same time, the PDP is the product of the quantum efficiency and probability that the primary e-h pair will trigger the avalanche. The former depends on a wavelength; the latter has a direct relation with the excess bias voltage, which is true for fast, free from diffusion tail, devices (see Figure 2.9).

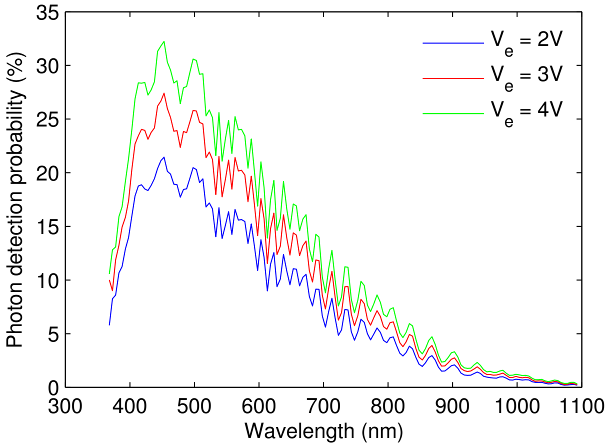

Figure 2.9: Typical photon detection probability curves of CMOS SPAD detector at different excess bias voltage [15].

Dark count rate and afterpulsing. Internal noise of the device is a characteristic which strongly affects the performance of the detector. It is called *dark count rate* (DCR) — that is, the avalanche triggering rate of the detector held in the darkness. The DCR has three constituents:

- thermal generation with a Poisson distribution and excess bias voltage dependence;
- generation caused by electron tunnelling from the valence band to the conduction band at a high field strength;
- *afterpulsing*, that is re-triggering of the avalanche in the absence of photon absorption caused by trap level generation.

The dark count rate caused by tunnelling is independent of the temperature but strongly depends on the excess bias voltage [22]. The thermal constituent of the dark count rate can be reduced by cooling down the detector; however, the lifetime of traps becomes longer in this case [23], [24]. The afterpulsing can be reduced by either increasing the *hold-off time*, which leads to worse performance in terms of time [24], or by decreasing the excess bias voltage, but this affects the photon detection efficiency [23].

A good example of the afterpulsing decreasing approach is the autotuning circuit for afterpulsing reduction in GM-APD proposed in [25]. The circuit, based on silicon delay lines, enabled the selection of the optimal hold-off time from 16 fixed times in 5–660 ns range. The autotuning did not require any interaction with the user or computer for selecting the optimum. The process completed in less than 20 sec.

All the characteristics described above, except the photon detection probability, depend on the quenching circuit being used. The purpose of the quenching circuit is to limit the maximum current flow through the device and to restore the device, so it can count subsequent photons.

Passive quenching. The simplest way to quench an avalanche is to connect the quenching resistor R_q in series with the cathode of SPAD, so it will stop the self-sustaining avalanche current (see Figure 2.10(a)) [26]. The avalanche current discharges the total capacitance C (made up by the sum of the junction capacitance C_j and the stray capacitance C_s) and induces the voltage drop over R_q. As it can be seen in Figure 2.10(b), the voltage on the diode decreases from the excess bias voltage V_e to the breakdown voltage V_{bd}. Then the voltage starts to restore slowly with the time constant R_qC.

During the recovery time, when the diode voltage is higher than the breakdown voltage but has not yet reached the intended final bias value, a photon can trigger an avalanche; however, the avalanche triggering probability depends on the time and is lower than that available at the final voltage. At the same time, the avalanche can be re-triggered by a trapped carrier (afterpulsing), increasing dark count rate, and worsen count rate. The pulses with amplitude smaller then the comparator threshold are dis-

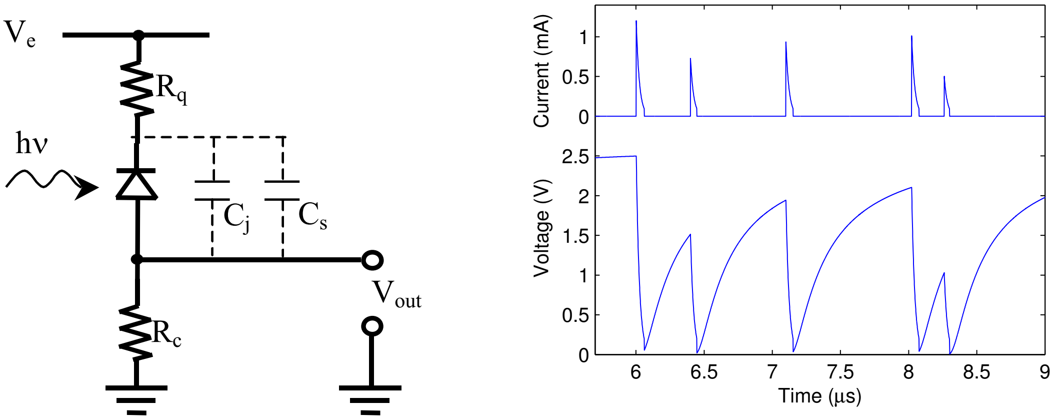

(a) Passive quenching circuit (b) Waveforms by passive quenching

Figure 2.10: a) The simplest passive quenching circuit with quenching resistor R_q in the order of a few hundred kΩ; b) waveforms of the avalanche current (upper) and of the voltage applied to SPAD (lower).

carded. It introduces a dead time but this time is not constant. This results in nonlinearity at hight count rates [22]. The drawbacks of the slow recovery can be diminished, but not removed, by reducing of the stray capacitance.

Active quenching. The active quenching (see Figure 2.11) does not have the drawbacks typical for the passive one. As soon as the avalanche is detected, the circuit forces the quenching by setting the bias voltage V_b to breakdown voltage V_{bd} or even below. After certain controlled time (named *hold-off time*), the bias voltage is reset to the initial state V_e by applying an additional voltage. It results in shorter quenching and recovery times then those in the case of passive quenching. The active quenching leaves an opportunity to deal with afterpulsing: the bias voltage can be put below the breakdown voltage and retained for a time sufficient to release the trapped carriers.

A comparison between passive and active SPAD recharge in terms of

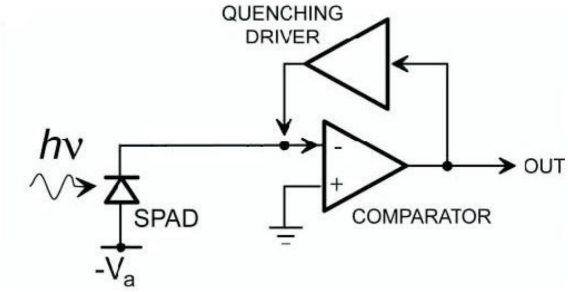

Figure 2.11: Schematic circuit diagram of the active quenching of SPAD [22].

time costs and afterpulsing is presented in Figure 2.12. The population of filled traps has an exponential dependence on time. With the passive recharge, the bias voltage V_b quickly reaches the avalanche threshold voltage, thus allowing afterpulsing. With the active recharge, V_b achieves the avalanche threshold voltage when the majority of traps have been released.

A comparison of the active and passive quenching is presented in Table 2.1.

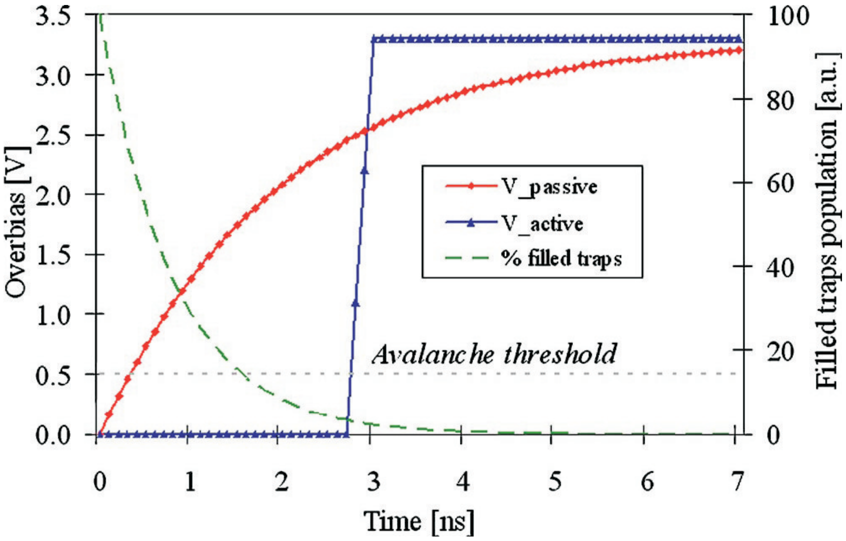

Figure 2.12: The recharge process in passive and active quenching circuits [27].

Table 2.1: Comparison of active and passive quenching.

Active quenching	**Passive quenching**
• Fixed and controlled dead time. • Shorter recovery time ⇒ higher count rate. • Adjustable hold-off time and afterpulsing.	• Simple to organize. • Long recovery time ⇒ smaller count rate. • Nonlinearity at high count rates. • Time dependent avalanche triggering probability.

2.3.1 State of the art SPAD characteristics

Performance comparison of different SPAD detectors is difficult not only because of the lak of unified criterion for performance estimation but also because the characteristics reported in the literature have been measured under different conditions (e.g. different Ve and temperature). Therefore, several devices with unique characteristics are presented below with the indication of used measurement conditions, where possible. A summary of the reviewed SPADs is presented in Table 2.2.

A small-area single SPAD with SiO_2 shallow-trench-isolation ring produced with 0.18 μm CMOS technology presented in [27] had dead time equal 3 ns. However, dark count rate was 200 kHz and photon detection efficiency was 11% at 450 nm. A similar SPAD reported in [28] had 26.7 ps FWHM and only 96.1 ps FW(1/100)M of time jitter.

For InGaAs/InP SPAD with 25 μm diameter, photon detection efficiency at 1310 ns was equal to 45% [29]. DCR was 70 kHz. The smallest time jitter for this device was 30 ps, measured at 6.5 V excess bias voltage. All characteristics were measured at 200K temperature.

Single SPADs with a double-epitaxial structure, large active area and fairly good photon detection efficiency were proposed in [19, 23]. Photon detection efficiency was 55% (at 500 nm) and 68% (at 550 nm) at V_e of 10 V, dark count rate was 1 kHz and 50 kHz (at room temperature) for active area diameters of 50 μm [19] and 200 μm [23], respectively. Both devices had 35 ps time resolution.

Richardson et al. [30] reported single SPAD with 8 μm diameter fabricated in 130-nm CMOS technology. The device had 20 Hz DCR at room temperature and PDP between 20% and 25% in range 440-570 nm (these values were received at 1 V bias). FWHM of time jitter was ~200 ps and the device demonstrated wavelength dependance of time resolution width below 30% of peak value. This dependance is explained by different absorption depth for photons with different energy.

A single SPAD implemented in high-voltage CMOS technology had sufficiently good characteristics and an interesting plateau in PDP(λ) dependence [31]. The peak value of PDP was 34.4% at 470 nm, and from 450 nm to 520 nm the PDP did not vary more than 1.5% from the maximum. Dark count rate for this device was 50 Hz at a temperature of 24°C. The time resolution was equal to 80 ps. All data were measured at $V_{bd} = 50$ V and $V_e = 5$ V.

A fully integrated system of 128×128 single photon avalanche diode sensors fabricated in CMOS technology has been presented in [32]. Maximum PDP was 35% and 40% at 460 nm and excess bias voltage of 3.3 V and 4 V, respectively. The median DCR across the whole device was 600 Hz at 20°C and peak-to-peak spreading over different single pixels was less than 100 Hz.

Pancheri and Stoppa [13] presented a 64-SPAD array fabricated in 0.35 μm high voltage CMOS with active area 15.8×15.8μm and 34% fill factor. Each pixel contained four single SPADs working in parallel and four time-gates with adjustable width in the range of 0.8 – 10 ns.

A 32×32 array of fully integrated SPADs with time-to-digital converters (one per pixel) was presented in [33, 34]. The detector was implemented in 130 nm CMOS technology. The time jitter of SPADs was 144 ps and of the entire system – 185 ps.

Table 2.2: The summary of observed SPADs.

Characteristic	**0.18**μm **CMOS [27, 28]**	**InGaAs/InP [29]**	**Single double-epitaxial [19, 23]**	**130**nm **CMOS [30]**
Area	2$\mu m \times 2\mu m$	$\varnothing$25 μm	$\varnothing$50, $\varnothing$200 μm	$\varnothing$8 μm
Dead time	3 ns	—	—	—
DCR	200 kHz	70 kHz	1 kHz, 50 kHz	20 Hz
PDP	11% at 450 nm	45% at 1310 nm	55%(500 nm) 68%(550 nm)	20% – 25% at 440 – 570 nm
Time response FWHM	26.7 ps, 96.1 ps = FW(1/100)M	30 ps	35 ps	200 ps
Characteristic	**HV CMOS [31]**	**0.35**μm **HV CMOS**[1]**[13]**	**130**nm **CMOS**[1] **[34]**	**0.35**μm **CMOS**[1] **[32]**
Area	—	15.8 × 15.8 μm	$\varnothing$10 μm	—
Dead time	—	200 ns	—	100 ns
DCR	50 Hz	1 kHz	100 kHz	600 Hz
PDP	34.4% at 470 nm	32% at 450 nm	34% at 450 nm	35% at 460 nm
Time response FWHM	80 ps	160 ps	144 ps	—

Different technologies have different advantages and disadvantages. The CMOS process, in comparison with dedicated technologies, usually produces SPADs with worse performance (in terms of DCR, PDP and afterpulsing). However, CMOS enables production of SPAD arrays with high fill factors. All silicon SPADs, irrespective of technology, are not suitable for detection of light with wavelengths higher than 1000 nm. In this case, InGaAs/InP SPADs with separate absorption, charge, and multiplication

---

[1] This is SPAD array

(SACM) structure should be used.

2.4 Summary

In this chapter the fluorescence process and its characteristics were considered. The methods of fluorescence detection in frequency and time-domain were described. The main focus was given to the time-correlated single photon counting and time-gating techniques of fluorescence decay measurement. We also discussed the operation principles of SPAD, their characteristics and features of quenching circuits. At the end the short overview of characteristics of modern single photon avalanche diodes was presented.

Chapter 3

State of the art of SPAD and fluorescence modelling

This chapter presents an overview of the previous works in the field of SPAD and fluorescence modelling.

In 1997, Spinelli and Lacaita [35] developed a 2-dimensional model of an avalanche spreading over the entire SPAD detector area. In their model, an avalanche multiplication process started from photon absorption point and then it spreaded by a diffusion-assisted process. The authors came to the conclusion that the timing resolution of a SPAD is limited by two factors: avalanche multiplication noise and spreading mechanism. Also, they found that photon-assisted spreading is negligible in comparison to the diffusion-assisted one. These modelling results are confirmed by the experimental results presented by Li and Davis [36], who found that a device with circular active area has the best time resolution when the light beam is focused in the center of the depletion region.

Kagawa [37] has shown theoretically that in Geiger-mode avalanche photodiodes the dark count probability decreases with the increase of multiplication layer thickness, while detection efficiency does not change. Three years later, Sugihara et al. [38] reported the existence of a critical thickness of the multiplication layer for GaInAs/InP single photon avalanche diodes.

Their numerical investigation shows that further increase of the multiplication layer thickness will rise the dark count probability. Similar results were reported by Ramirez and Hayat [39]. There, the authors investigated the behaviour of DCR and PDP in two modes: at low temperature, when the field-assisted mechanism of dark carriers generation is dominant, and at room temperature, when dominates the generation/recombination mechanism. For the first case, the increase of the multiplication layer thickness results in improvements of PDP versus DCR. In the second case, the PDP versus DCR characteristics showed weaker performance with the growth of the multiplication region.

An analytical model of dark count probability and single-photon quantum efficiency was proposed by Kang et al. [40]. The model linked these performance parameters with other SPAD parameters and operation conditions, such as detrap time constant, gain-bandwidth product, gate repetition rate, etc.

Jackson et al. [41] calculated the theoretical minimum dark count rate at the room temperature for 20 μm Geiger mode avalanche photodiode. The model used for this calculation was based on the analytical solution for dark counts from [42] and the results from commercially available process and device simulators. The authors found that the minimum dark count rate for a 20 μm device with defect-free depletion region is around 30-40 Hz. Later, temperature dependence of dark counts was measured by Jackson et al. [43] for the same device. They found that the dark count rate increases by an order of magnitude per each 20°C for the temperature range between -10°C and +25°C (the measurements were performed with the detector biased at 10 V above breakdown and with 125 ns hold-off time). On the other hand, the decrease of the detector temperature increases the trap lifetime and thus afterpulsing. However, this effect was not observed in [43] due to long hold off time used in the measurements.

The optical crosstalk, as a limiting factor for fabrication of high-density SPAD arrays, has been investigated in several works. Jackson et al. [44] considered the optical crosstalk as light propagation between SPAD pixels through direct optical paths. Two– and three–dimensional models of optical coupling between two adjacent pixels were developed. The model considered the light absorption in silicon, the photon emission was considered as a function of reverse bias current. The emitting detector was assumed to be a point source with a spherical photon flux. By simulation and measurements, Jackson et al. demonstrated that by separating the pixels by 330 μm the optical coupling reduces almost to dark count level, without any additional optical isolation. Later, Rech et al. [45, 46] shown that even with optical isolation (in that case, a deep phosphorus diffusion surrounding the detector) the optical crosstalk in SPAD arrays can not be completely prevented. It happens because of indirect optical paths that also take place. An example of the indirect optical path is the internal reflection from the bottom silicon–air surface. A 3-D optical model of the optical crosstalk caused by indirect optical paths was presented in [46]. The model confirmed the hypothesis of presence of the crosstalk component caused by the internal reflection and estimated the wavelength range which makes a significant contribution to this component: between 1100 and 1200 nm.

Köllner and Wolfrum [47] made a theoretical calculation of the minimum number of photon counts which is essential to achieve the desired accuracy in lifetime estimation:

$$N \geq \frac{\mathrm{var}_1(\tau)}{\text{desired variance}(\tau)}, \tag{3.1}$$

where $\mathrm{var}_1(\tau)$ is the variance of τ in case when only one photon per channel is detected. This expression has been derived for the case of multinomial statistics of counts. However, the distribution of number of counts by channels is usually described by a Poisson distribution [48, 49]. Köllner and Wolfrum state that the multinomial approach is applicable to the least-square approach with Poisson statistics in most cases, when the relative error in N, i.e. $1/\sqrt{N}$, is small. The optimal experimental conditions, such as the measurement time interval T and the number of channels with equal width, were investigated for monoexponential decay in absence of background noise. It was demonstrated that in the case of 2 channels the optimum measurement interval T is 5τ; consequently, the channels width is 2.5τ. In the case of T longer than 10τ, the increase of the number of channels bigger than 8 does not provide any profits in terms of minimum number of counts per channel.

Gerritsen and colleagues continued the previous work and investigated the influence of more than two observation windows with constant and different width, on lifetime resolution [50, 51, 10]. Simulation with a very simple model (random counts were accumulated in gates according to the delay probability function $P(t) = \tau e^{-t/\tau}$ and delay between the excitation pulse and the first gate of 0.5 ns, which simulates the detector response time) provided the following results:

- the detection with four time-gates is more sensitive than with two;
- the detection with more than four time-gates demonstrates smaller sensitivity difference in comparison with four-gate detection;
- the detection with non-equal gate widths has certain advantages, because narrow first gates are mainly sensitive to short lifetimes, wider late gates — to longer ones, and thus a mixture of fluorophores with different lifetimes can be distinguished;
- the statistics of the lifetime measurements is dominated by Poisson noise.

The simulation results were confirmed by real experiments.

Palo et al. [52] presented theoretical count-number distributions for fluorescence intensity distribution analysis (FIDA). FIDA is outside of the scope of our project, but the approach used to create the model in [52] is applicable for our task of fluorescence sample simulation. The model proposed in [52] considers the diffusion of the studied molecules, singlet-triplet transitions (which make the molecules “invisible” from the fluorescence point of view), and fluorescence emission. For the specific case of no-diffusion, the model has been solved analytically, while for more general cases the numerical solutions were used. The authors also estimated the correction for afterpulsing and dead time of the detector.

A number of publications from Davis and colleagues [53–57] present a Monte Carlo simulation of a single-molecule detection experiment. In that simulation, an almost comprehensive model of biological sample has been built. The model considers fluorophore excitation including polarization and saturation effects, photodegradation due to intersystem crossing to triplet state, triplet and singlet state relaxation (phosphorescence and fluorescence, respectively). The authors also performed a simulation of laser intensity, light collection system and detection, including data processing. The simulated results demonstrated a good qualitative agreement with the experimental data while the clear quantitative comparison is absent.

The project described above is somewhat similar to our work, however, there are a number of substantial differencies. First of all, the authors focused on detection of the fluorescence itself, while we consider also the characteristics of the detected fluorescence, such as lifetime. Then, they model the physical processes with a fixed time step, while our model is event-driven and considers exact timing of each photon in a subnanosecond scale. It should also be noted that the studied experiments have differences in the setup, which are reflected by the respective model. For example, the model of Davis et al. comprises an optical system, which in our experiments was represented only by a filter. On the other hand, they employ only a basic simplified detector model based on averaged empirical parameters (such as constant dead time for a passively quenched SPAD, and single PDP value independent of wavelength). Our model, in contrast, takes into account the inner processes in SPAD and evaluates the behaviour of the device from its characteristics. For example, we model afterpulsing as a time-dependent probability distribution, while Davis et al. consider it to be a constant time-independent value.

As it can be seen from the above, modelling of fluorescence processes and SPAD detectors can yield new knowledge and explain some experimental results. However, most of the projects focused on modelling of a limited subset of the experimental setup. The only complete model is dedicated to a different type of experiment and lacks the details of physical processes in the detector. So far, there was no general model considering in detail all the parts of a fluorescence lifetime measurement experiment.

Chapter 4

The simulation model of fluorescence measurement experiment

4.1 Simulation modelling

One of the essential features of science is the complexity of systems under investigation. To be able to work with this complexity, researchers construct a model of the investigated system including into consideration only essential parts and properties of interest. The model used to describe an object can be physical (simplified physical prototype) or mathematical one (i.e., a system of formal concepts describing the real object with the required level of detail). In turn, mathematical models divide into two classes: analytical and simulation models.

The analytical modelling can be used when the mathematical model is simple enough and can be expressed in analytical formulas. The advantages of this type of modelling are high precision, consideration of entire classes of the systems, discovery of the most general principles of the systems. However, many systems are highly complex, so the creation of analytical models is impossible or requires so many assumptions and simplifications that the estimations obtained via modelling are unsatisfactory. In these cases simulation modelling offers an alternative.

A simulation modelling algorithm simulates system behaviour by taking into account external influences and interaction of distinct system elements. It should be noted, that both the external influences and interaction of distinct elements can have either deterministic or stochastic nature. The estimation of system parameters is performed by carrying out series of statistical experiments with the simulation model, data accumulation and their subsequent processing.

In comparison to the analytical modelling, the simulation one is less universal. Simulation models are usually tailored to specific systems, and unlike analytical models they cannot reveal general principles of entire classes of systems. On the other hand, simulation modelling is capable of modelling systems of virtually any complexity. In many cases simulation modelling is the best or the only possible way to study the system of interest — the cost of simulation modelling is usually significantly less than that of a natural experiment, while the modelling results remain in a good agreement with real experiments.

Table 4.1: The main advantages and disadvantages of simulation modelling.

Advantages	**Disadvantages**
• Systems of virtually any complexity can be modelled. • It is sufficient to know only the behaviour of system elements to simulate interaction between them. • Majority of the parameters have a physical meaning.	• It cannot reveal general principles of entire classes of systems. • The stochastic nature of the simulation modelling results in smaller precision. • Simulation experiments can be time consuming, depending on computational resources.

Table 4.1 summarises the most important properties of the simulation modelling, its advantages and disadvantages.

The simulation modelling is a powerful tool of modern research, its applications can be found in various areas, such as biology [58], agriculture [59], economics [60], chemistry [61], physics [62], computer networking [63], etc.

The described features the simulation modelling have motivated us to choose it as the main tool for this work.

4.2 General overview of the model

The model of a fluorescence measurement setup consists of a set of independent modules. Each of them simulates the corresponding parts of the experiment. A schematic diagram of the units, their inputs and outputs are shown in Figure 4.1.

The idea of simulation is to create an array of photons at the beginning and then to change the time and wavelength values of the individual photons as they pass through the system. At some stages the amount of photons is also changed (for example, it is decreased during fluorescence simulation because of absorption without subsequent radiation). The array of photons from the previous simulation unit is one of the inputs of the next unit. This type of simulation workflow is called *forward simulation.*

Depending on many factors, the fraction of photons that reach the detector varies from units to tens of percents of the initially generated set. This means that the time spent on generation and processing of more than half of photons has been wasted.

To minimize the simulation time, we have reversed the direction of simulation workflow. With the *backward simulation*, only the “survived” photons are generated at the beginning of the modelling and each simulation unit changes only the time and wavelength characteristics of the photons but not their quantity. This approach reduces the calculation time and

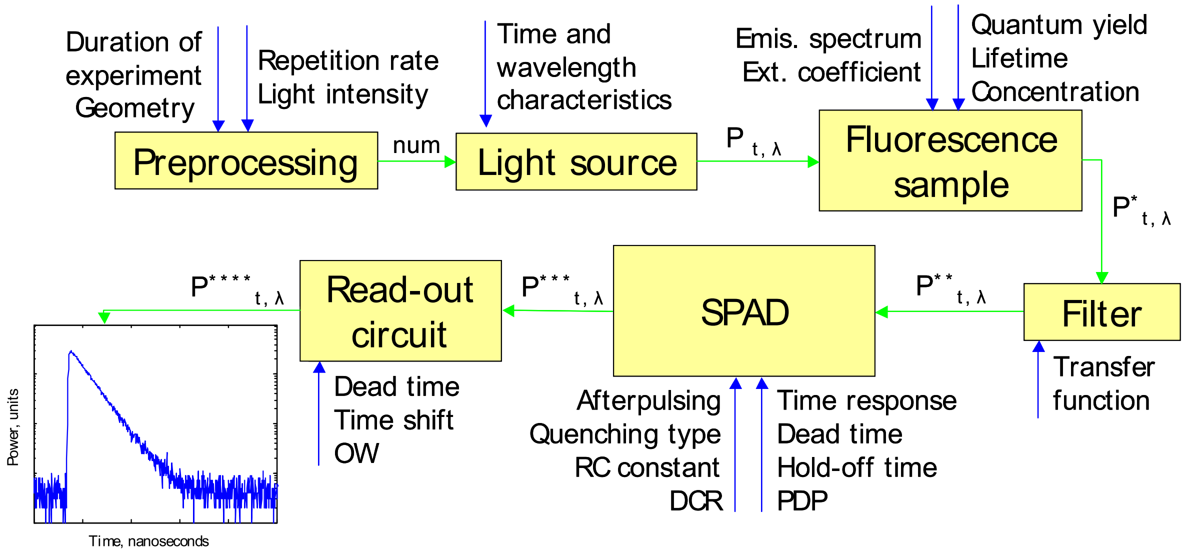

Figure 4.1: Schematic diagram of the simulation model. Blue arrows represent experimental parameters.

enables simulation of longer and more complex experiments.

Backward simulation is made possible by combining all the factors that change the number of photons into a single coefficient. This *loss coefficient* includes:

- filtering,
- absorption by a fluorescent sample without following radiation,
- geometrical losses,
- losses due to finite SPAD detection area.

The following sections provide a detailed description of each of the simulation units.

4.3 Preprocessing

The number of photons generated during a typical fluorescence measurement experiment can easily exceed the memory capacity of any computer.

Thus, it is often infeasible to simulate the whole experiment in one run. The preprocessing unit solves this problem by splitting the whole experiment duration into smaller periods, depending on the setup geometry, light intensity, measurement technique and the available computational resources. It also calculates the number of photons that must be generated in the light source simulation unit.

The inputs of the preprocessing unit are:

- duration of the experiment,
- measurement technique,
- light source characteristics (repetition rate of the light source (synchronizing pulses); intensity, mean wavelength, divergence and diameter of the light beam; duration of the light pulses),
- parameters of the fluorescent sample and filter,
- geometry of the experimental setup (distance between light source and fluorescence sample, fluorescence sample and detection surface; SPAD active area; dimensions of fluorescence sample).

The preprocessing starts with the calculation of the number of photons per one light pulse:

$$N_0 = \frac{I \Delta t}{hc/\lambda}, \tag{4.1}$$

where I is the pulse light intensity (W), Δt is the duration of the light pulse (s), h is the Planck constant (Js), c is the speed of light (m/s) and λ is the mean wavelength of the light pulse (m).

The number of photons that will reach the detector is calculated as the product of N_0 and the loss coefficient. It should be noted that the loss coefficients for excitation (initial) and fluorescent photons are calculated separately. The components L_i of the loss coefficients are presented in Table 4.2. The total loss coefficient is the product of its components.

Thus, the number of the excitation photons that reach the detector is

$$N_l = N_0 L_2 (1 - L_3/QY) L_4 \tag{4.2}$$

and the number of fluorescent photons reached the detector is

$$N_f = N_0 L_1 L_3 L_5. \tag{4.3}$$

The total number of photons reaching the detector per single light pulse ("survived" photons) is the sum of these components:

$$N = N_l + N_f. \tag{4.4}$$

Taking into account the number of "survived" photons per one pulse, the preprocessing unit calculates the number of pulses considered in one pass of the simulation and the corresponding time interval as

$$N_{pl} = \lfloor \frac{N_{opt}}{N} \rfloor, \tag{4.5}$$

$$\Delta t = \frac{N_{pl}}{f}, \tag{4.6}$$

where N_{opt} is the optimal array length for MATLAB operation depending on the available computational resources[1], f is the light repetition rate (frequency) of pulses. The number of passes depends on the duration of the experiment T and the chosen measurement technique.

For TCSPC the number of passes is

$$N_p = \lceil \frac{T}{\Delta t} \rceil. \tag{4.7}$$

In the case of time-gating, the number of passes is

$$N_p = \lceil \frac{OW}{\Delta t} \rceil \times \lceil \frac{1/f - OW}{t_{sh}} \rceil, \tag{4.8}$$

---

[1] Empirically found estimates of N_{opt} are 10^5 for 1 GB RAM and 10^7 for 4 GB RAM.

where OW and t_{sh} are the observation window and time shift for time-gating. Finally, the number of photons that should be generated in the light source simulation unit per single pass is calculated as

$$N_g = N_{pl}N. \tag{4.9}$$

Table 4.2: The components of the loss coefficients[2].

Definition	**Equation**	**Description**
Losses between light source and fluorophore planes due to beam divergence. Losses between light source and detector planes due to beam divergence.	$L_1 = min(1, l_1)$ $l_1 = \left(\frac{R_f}{d_{lf}tg(\alpha/2)+r}\right)^2$ $L_2 = min(1, l_2)$ $l_2 = \left(\frac{R_d}{d_{ld}tg(\alpha/2)+r}\right)^2$	R_f and R_d are the effective radiuses (cm) of lighted area of fluorescent sample and active detection area, correspondingly; d_{lf} and d_{ld} are the distances (cm) between light source and fluorescent sample, light source and detection planes, correspondingly; r is the radius (cm) of the light beam; $\angle\alpha$ is the beam divergence (°).
Losses caused by non-radiation absorption in fluorescence sample (see Section 4.5).	$L_3 = QY(1 - 10^{-\varepsilon cl})$	ε is the molar extinction coefficient ($M^{-1}cm^{-1}$), c is the fluorophore concentration (M), l is the thickness (cm) of fluorescent sample, QY is the quantum yield of fluorophore.
Filter losses.	$L_4 = 1 - T$	T is the filter transmittance on light source peak wavelength.
Losses between fluorescent and detection planes because of spatially uniform fluorescence emission and finite detection area.	$L_5 = S_d/(4\pi d_{fd}^2)$	S_d is the active detection area (cm^2), d_{fd} is the distance (cm) between fluorescent and detection planes.

---

[2] The calculations presented in this table are theoretical and have not been verified experimentally.

The output of the preprocessing block is the number of photons N_g to be generated in each pass of the simulation.

4.4 Light source simulation

The light source simulation unit generates an array of photons according to the time and wavelength characteristics of the light source.

The input of the light source simulation unit consists of the time and wavelength characteristics of the light source and the number of photons to generate N_g, provided by the preprocessing unit (see Section 4.3). If the spectrum and time curves are not available, they are approximated as a 2-dimensional normal distribution. In this case, the full width at half of maximum (FWHM) and the peak value for time curve and spectrum must be provided as inputs. The approximation function has the following form:

$$f(t, \lambda) = \frac{1}{2\pi\sigma_t\sigma_\lambda} \exp\left(-\frac{1}{2}\left[\frac{(t-\mu_t)^2}{\sigma_t^2} + \frac{(\lambda-\mu_\lambda)^2}{\sigma_\lambda^2}\right]\right) \tag{4.10}$$

where μ_t, μ_λ and σ_t, σ_λ are the mean values and the standard deviations of time and frequency, respectively. The standard deviations are calculated as [64]

$$\sigma = \frac{FWHM}{2.35482}. \tag{4.11}$$

For curves shaped similarly to normal distribution the error of such approximation does not exceed 15%. This error value has been calculated as

$$R = \sum_{i=1}^{n} \frac{|S_i - E_i|}{S_i + E_i} \tag{4.12}$$

where S_i and E_i are the simulated and empirical values on i$^{\text{th}}$ interval, n is the number of intervals.

The array of photons is generated using the rejection method [65], which allows modelling of any empirically or analytically defined curves. To optimise the generation time, we limit the rejection method to work within predefined bounds. For the analytical probability density function (PDF) specified by the Gaussian (4.10), the generation interval is selected as $[\mu - 3\sigma,\ \mu + 3\sigma]$. The error of such approximation is less than 1% [66, p. 88]. For empirical functions, defined by their values in certain points, the generation interval bounds are set at the level corresponding to 1% of the peak value. The error in this case is around 1%[1].

Some examples of the light source simulation are presented in Figure 4.2. The blue micro-LED produced by the University of Strathclyde [67] and Picoquant LDH-P-C-470 pulsed diode laser with 80-ps FWHM [68] were used as light sources. The average LED and laser powers were 2.7 μW and 5.9 mW, respectively. The measured graphs were obtained with TCSPC card. The simulated graphs were obtained from histograms of the simulated photons, scaled to the peak of the corresponding measured graphs.

In the case when the modelling was performed on the base of empirical curves, the simulation error was 0.4% and 0.8% for micro-LED and laser, respectively. The approximation by the normal distribution resulted in the error of 12% for micro-LED, while for laser the error was 53%. Obviously, such an approximation in the case of laser is unsatisfactory and the simulation based on empirical curve is preferable. Alternatively, a more complex approximation can be used — for example, a mixture of two or more Gaussians.

4.5 Fluorescence simulation

The inputs of the fluorescence simulation unit are the concentration of fluorophores (M), quantum yield, molar extinction coefficient ($\mathrm{M}^{-1}\mathrm{cm}^{-1}$),

---

[1] This estimate has been calculated on the base of the data for a blue micro-LED produced by the University of Strathclyde [67] and Picoquant LDH-P-C-470 pulsed diode laser with 80-ps FWHM [68].

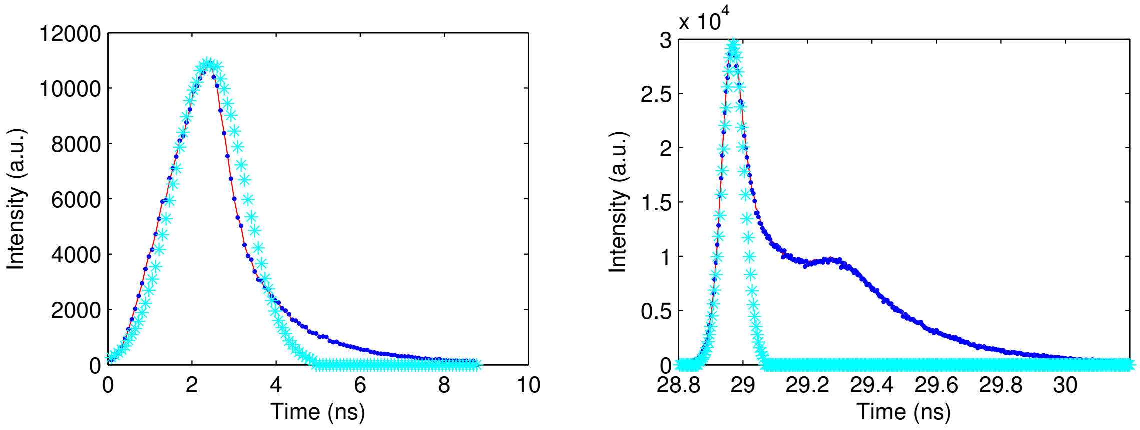

(a) Micro-LED (b) Laser

Figure 4.2: Light source simulation. The red solid line is the empirical time characteristic, the blue dots is the simulated time characteristic based on empirical curve and the cyan asterisks are the simulated time characteristic with Gaussian distribution as the first approximation.

emission spectrum and thickness of fluorescent sample. For the simulation of the fluorescent sample, the following assumptions have been made:

- the light absorption obeys the Beer-Lambert law;
- fluorophores have uniform distribution;
- the optical density of the fluorescent sample is negligible;
- fluorescence decay is monoexponential;
- there are no other processes besides fluorescence.

These assumptions considerably decrease the computation times and at the same time they are still in a good agreement with the real world.

The number of absorbed photons is calculated based on extinction coefficient ε, fluorophore thickness l and concentration c by Beer-Lambert law [7, sec. 2.13]

$$N_a = (1 - 10^{-\varepsilon c l}) N_c \,, \tag{4.13}$$

where N_c is the number of photons arrived to the fluorescent sample. The number of emitted photons is determined by the quantum yield (QY) of the fluorophore

$$N_e = N_a QY, \tag{4.14}$$

However, considering the fact that the simulation is of backward type, the losses caused by the absorption without consequent emission have already been taken into account at the preprocessing step. On the current step we have an array P of N_g photons, where N_f/N of them are fluorescent photons (see Section 4.3). All photons are identical from the fluorescence point of view. Therefore, the fluorescent photons should be picked from array P. In order to do that, the system generates an array r of random values uniformly distributed in range $[0, 1]$. The length of this array is equal to the number of generated photons, i.e. N_g. The fluorescent photons are then chosen by the following criterion

$$\forall\, r_i,\ i \in \overline{0, N_g},\ P_i = \begin{cases} \text{fluorescent photon,} & r_i < N_f/N \\ \text{passed photon,} & r_i \geq N_f/N \end{cases} \tag{4.15}$$

New time and wavelength values are then simulated for each fluorescent photon. Time increments are generated by the inverse function method [69, sec. 4.2]:

$$\Delta t_j = -\tau \ln z_j \tag{4.16}$$

where τ is the fluorophore lifetime, z is a random variable uniformly distributed on [0,1], j is the index of the photon, varying from 1 to the total number of fluorescent photons. The new time value is the sum of the previous time value and the time increment

$$t_j = t_j + \Delta t_j.$$

New wavelengths are generated by a rejection method according to the emission spectrum of the fluorophore.

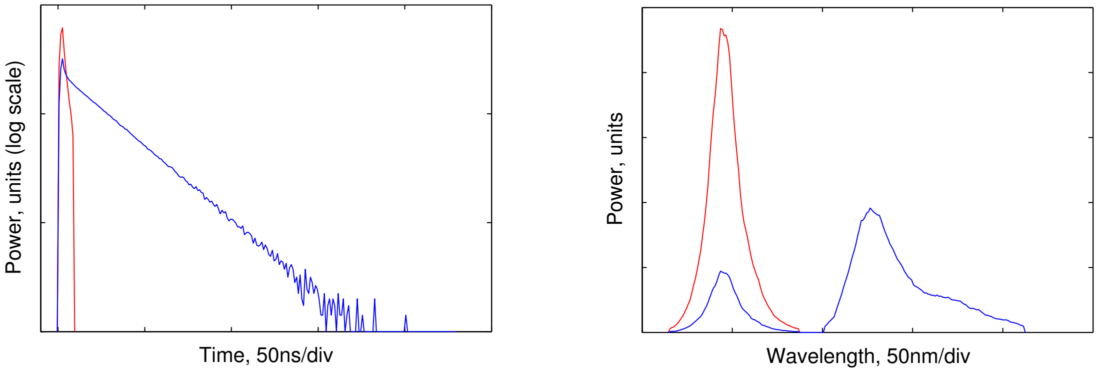

(a) Time curve (b) Spectrum

Figure 4.3: Fluorescence simulation. The time curve and the spectrum are shown for exciting (red curve) and fluorescent light (blue curve).

The output of the fluorescence simulation unit is an array of both the fluorescent photons with updated time and wavelength values, and the passed photons with unchanged characteristics.

An example of fluorescence simulation is presented in Figure 4.3. Micro-LED with FWHM=1.7 ns (see Figure 4.2(a)) was used as a light source. Fluorescence lifetime was 16 ns. The ratio between fluorescent photons and the total number of photons N_f/N was 0.8. This ratio can be seen in the spectrum in Figure 4.3(b): the first peak of the fluorescent spectrum corresponds to the passed photons and accounts for 20% of the exciting spectrum.

4.6 SPAD-based detector simulation

The SPAD simulation unit models detector noise, including afterpulses and the detection of incoming photons with corresponding time response. The input of the SPAD simulation unit comprises:

- dependence of photon detection probability (PDP) from wavelength,

- time response curve,
- dark count rate (DCR) value,
- afterpulsing time distribution,
- type of quenching circuit with its characteristics.

The block diagram of the SPAD simulation is shown in Figure 4.4.

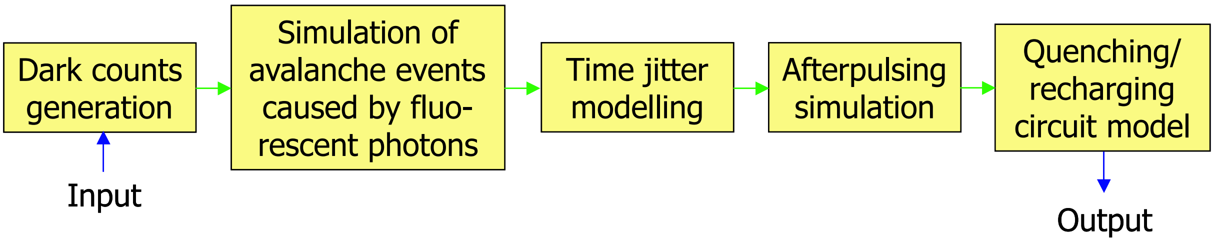

Figure 4.4: The block diagram of SPAD simulation.

Dark count rate. The SPAD simulation starts with the generation of dark counts. It is modelled as a Poisson flow with the rate parameter equal to the DCR value of the detector. The occurrence times are defined by the following recurrent equation:

$$t_0 = t_{beg}, \quad \forall\, t_i \le t_{end}, \quad t_i = t_{i-1} - \ln r_i / \lambda, \tag{4.17}$$

where λ is the rate parameter of Poisson flow, r_i is a realization of a random variate uniformly distributed on $[0, 1]$, t_{beg} and t_{end} are the start and the end of the time interval (4.6) on this pass. It should be noted, that t_0 is not a random variable and is not a dark count event, it is used just to initiate the noise modelling.

An example of the noise simulation with DCR=100 Hz is demonstrated in Figure 4.5. Figure 4.5(a) shows the first 10^3 of 10^6 realisations of DCR modelling. Figure 4.5(b) presents a comparison of simulated and theoretical PDFs for all realisations. This simulation has been verified by the

Pearson's χ^2 test [70] and the resulting p-value was 0.36, which proves the high simulation accuracy.

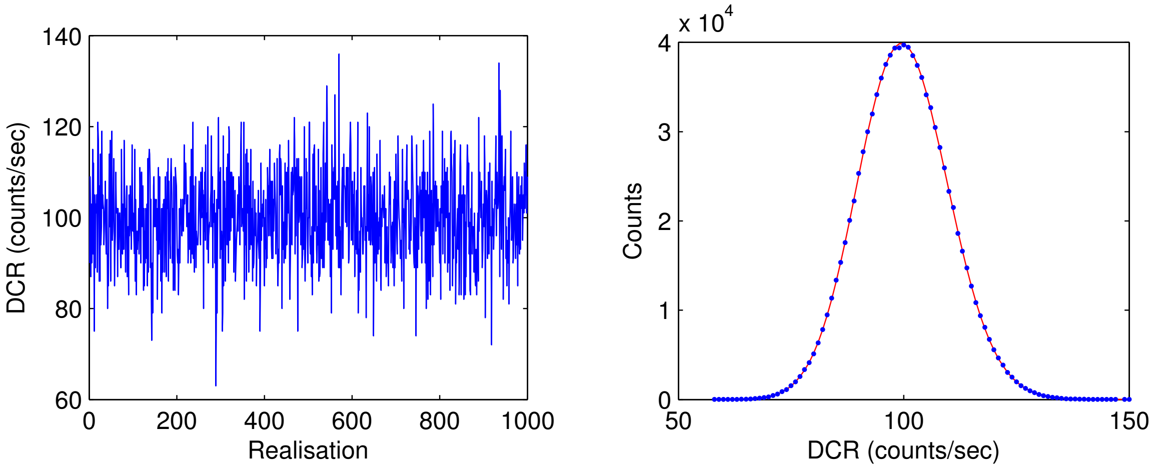

(a) DCR simulation

(b) PDF

Figure 4.5: Dark count rate simulation. a) Simulated DCR for 10^3 realisations. b) A comparison of simulated (blue dots) and theoretical (red solid line) PDF of noise for 10^6 realisations.

Photon detection probability. The next step of the SPAD simulation is the modelling of avalanche triggering caused by incoming photons in accordance to the PDP. At the beginning of this step a random variate r, uniformly distributed on $[0, \max(PDP)]$, is generated for each photon. Then, r is compared to the PDP for the photon's wavelength. The photon is considered as detected if $r < PDP(\lambda_p)$. For such a photon, the detection time is calculated as the photon arrival time plus detector response time, which is generated by rejection method in accordance to the time response characteristic of the detector.

Afterpulsing. At the next step, the afterpulsing probability P_{aft} is calculated on the base of DCR, dead time and afterpulsing characteristic of the detector. In the case of passive quenching the dead time is zero, while in the case of active quenching the dead time is the sum of the physical dead time and hold-off time (see Section 2.3). In graphical representation, the afterpulsing probability is the area between DCR level and afterpulsing curve, bounded by the dead time (see Figure 4.6).

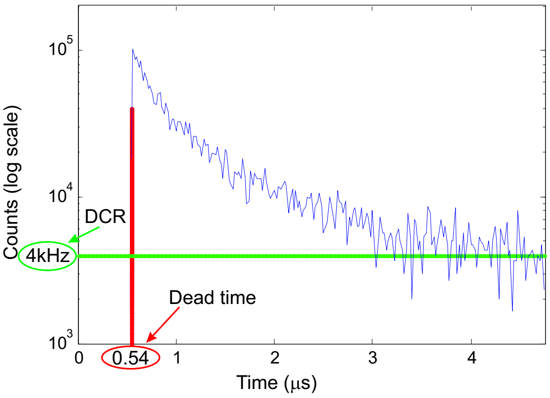

Figure 4.6: Afterpulsing probability calculation[1].

The described approach is more flexible than a straightforward use of the fixed value of afterpulsing probability (provided as input parameter). For example, if one wants to analyse how hold-off time influences the noise characteristic, one needs to change only the parameter of interest — the afterpulsing probability will be recalculated automatically.

To simulate afterpulses, a random variate r, uniformly distributed on $[0, 1]$, is generated for each photon. The afterpulses occur for those photons for which $r < P_{aft}$. The times of afterpulses are generated by rejection method, in accordance to the afterpulsing curve. The generated interval spans from the dead time to the time where the afterpulsing curve converges to the DCR level (around 3.5 μs for the curve in Figure 4.6).

An example of the afterpulsing simulation is presented in Figure 4.7. Afterpulsing of SPAD CMOS sensor reported in [15] has been simulated

---

[1] This afterpulsing curve was measured for SPAD CMOS sensor reported in [15]. The real dead time of this SPAD was 520 ns and there was 20 ns additional delay applied externally. So, the afterpulsing events appeared after 540 ns.

for 10^7 photons. The reported and simulated afterpulsing probabilities were 4.5% and 5.2% respectively.

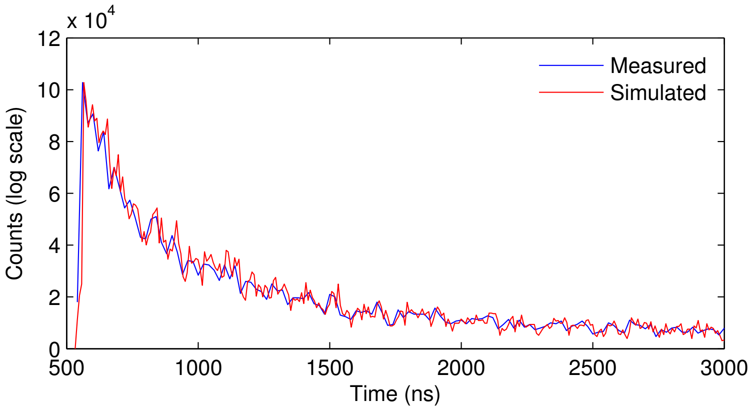

Figure 4.7: An example of afterpulsing simulation.

All the detected photons, dark counts and afterpulses are combined into one array D and sorted by time in the ascending order. The last step of the SPAD simulation performs pruning of these events in accordance to the quenching/recharging circuit functionalilty.

Active quenching. In the case of active quenching/recharging, the SPAD has a fixed time interval after detection; during this period the detection of the next event is impossible. This time interval consists of the physical detector dead time and the hold-off time (see Section 2.3). All the events from the array D related to that time period are excluded from further consideration. The remaining times are the output of the SPAD simulation unit. The block diagram of active quenching is depicted in Figure 4.8.

Passive quenching. In the case of passive quenching/recharging, the SPAD does not have a fixed dead time. Current and voltage pulses are now produced for each triggering event, but with different amplitudes which depend on the time elapsed from the previous event (see Figure 2.10(b)).

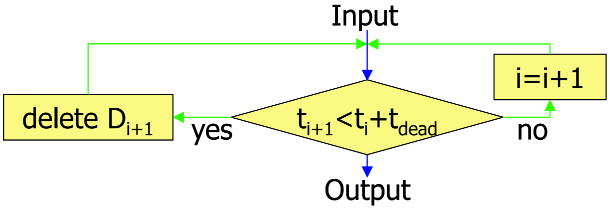

Figure 4.8: Active quenching/recharging simulation.

However, a comparator at the output has a threshold level and the pulses with smaller amplitudes are discarded.

To simulate such a behaviour, we first calculate the time distances Δt between two consecutive events in the array D. The amplitude of the first current/voltage pulse caused by the first event from array D is assumed to be the maximum value. The amplitudes of all the consequent current/voltage pulses are calculated as

$$A_i = A_{max} \exp(-RC/\Delta t_i), \tag{4.18}$$

where A_{max} is the maximum value of the pulse, Δt_i is the time interval between i^{th} and $(i-1)^{\text{th}}$ events, R is the resistance of the quenching resistor and C is the total capacitance at the diode terminal (see Figure 2.10(a)). All events with amplitudes smaller than the comparator threshold ($A_i < A_{th}$) are not considered in the further processing. The remaining event times are the output of the SPAD simulation unit.

The simulated current pulses of the SPAD with passive quenching are shown in Figure 4.9. The figure presents the cumulative picture of pulses occurred at different times after the previous avalanche event. The amplitude envelope corresponds to the voltage recovery graph (see Figure 2.10(b)).

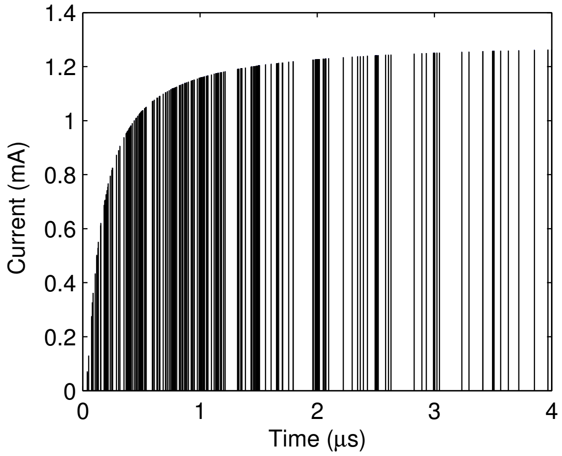

Figure 4.9: The simulated current pulses of the SPAD with passive quenching.

4.7 Measurement technique simulation

TCSPC. In the case of time-correlated single photon counting the first photons (ideally, single photons) per signal period should be detected (see Section 2.3). In real experiments the synchronization signal is provided by the light source. In the model it is simulated in the following way.

At the input this module receives an array D which contains the absolute times of detected events. Integer division of vector D by signal period (time between two consecutive light pulses) gives sequence S of sets of equal numbers where value is serial number of the signal period and set length is the number of events detected in this signal period.

$$S_i = \lfloor \frac{D_i}{1/f} \rfloor, \tag{4.19}$$

where f is the light repetition rate (frequency). The indexes of the first unique numbers in this sequence are the indexes of events which are the output O of TCSPC in absolute time. To obtain the times in the signal period interval the remainder of division of absolute time by signal period should be taken

$$T_j^{TCSPC} = \text{rem}\left(\frac{O_j}{1/f}\right). \tag{4.20}$$

An example of the TCSPC simulation is presented in Figure 4.10.

$$\begin{array}{rcccccccccccc}
D = & D_1, & D_2, & D_3, & D_4 & \dots & D_{k-2}, & D_{k-1}, & D_k, & D_{k+1} & \dots & D_{m-2}, & D_{m-1}, & D_m \\
S = & 0, & 1, & 1, & 2 & \dots & i-1, & i, & i, & i+1 & \dots & N_{pl-1}, & N_{pl}, & N_{pl} \\
O = & D_1, & D_2, & & D_4 & \dots & & D_{k-1}, & & D_{k+1} & \dots & & D_{m-1} &
\end{array}$$

$$\downarrow$$

$$O = \quad D_1, D_2, D_4, \dots, D_{k-1}, D_{k+1}, \dots, D_{m-1}$$
$$T_{TCSPC} = rem\left(\frac{D_1}{1/f}\right),\ rem\left(\frac{D_2}{1/f}\right),\ rem\left(\frac{D_4}{1/f}\right),\ \dots$$

Figure 4.10: An example of TCSPC simulation.

In practice, the TCSPC module can count more that one photon per light pulse. When the probability of detection of multiple photons per light pulse is high, the dead time of the TCSPC module becomes a significant parameter and should also be included into the simulation. However, if the TCSPC dead time is smaller than the detector dead time, it can be neglected.

Time-gating. For the simulation of time-gating measurement technique, the inputs of this simulation unit are composed of a set of the time shifts and initial observation windows (OW). The positions of the OWs for the subsequent passes are calculated as

$$OW_h^k = \begin{cases} OW_h^1 + (k-1)t_{sh}, & \text{if } t_{sh} = \text{const} \\ OW_h^1 + t_{sh}^k, & \text{if } t_{sh} \neq \text{const} \end{cases} \tag{4.21}$$

where h is the number of OW, k is the number of the simulation pass (from 2 to N_p (4.8)), OW_h^1 is OW_h at the beginning of the simulation, t_{sh} is the time shift at the k^{th} simulation pass. Then, we calculate the number of photons detected during each OW

$$T_h^{TG} = |D \in OW_h|, \tag{4.22}$$

where D is the array of all detected events at the simulated time interval Δt (4.6).

4.8 Model implementation

The described model has been implemented in MATLAB® 7. The model input parameters are specified in two ways. Single parameters, like DCR level and fluorophore QY, are provided through the graphical user interface (GUI) shown in Figure 4.11. When the user clicks the "Run" button, these parameters are automatically saved into a dedicated m-file, from which they can be accessed when required. Complex parameters, such as fluorescence emission spectrum and SPAD time jitter curve, are stored into the same m-file by a special function. The simulation speed depends both on the modelling parameters and the available computational resources.

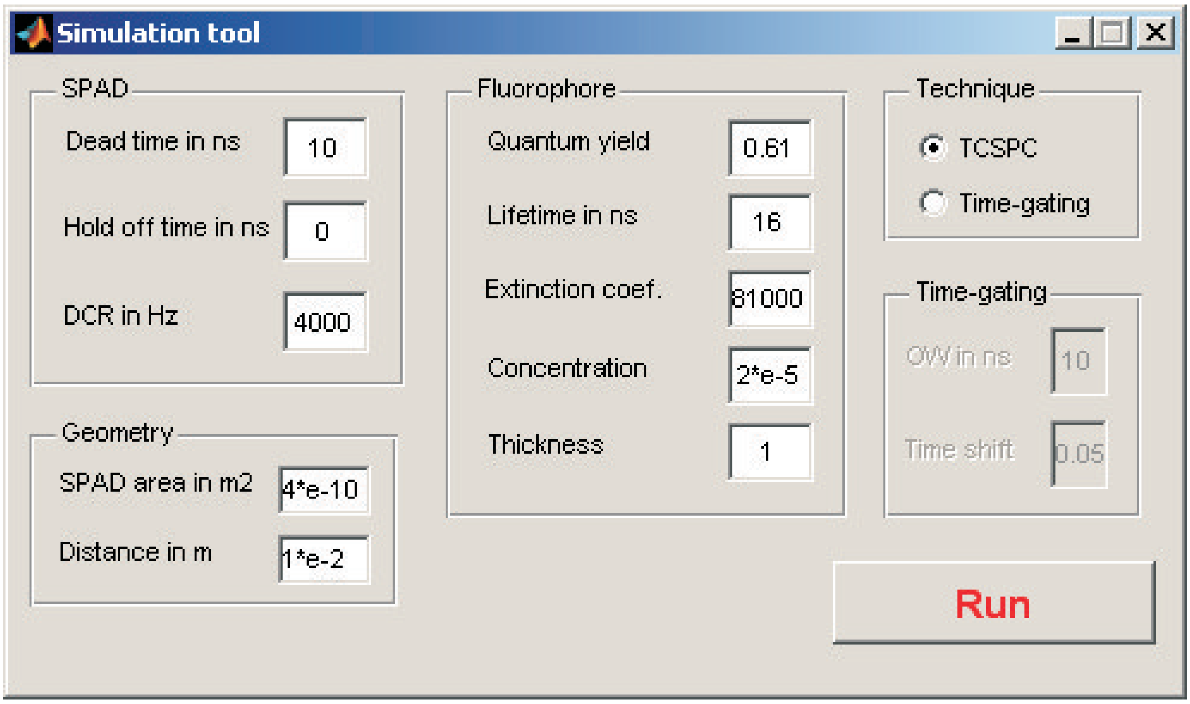

Dead time in ns 10
Hold off time in ns 0
DCR in Hz 4000
SPAD area in m2 4*e-10
Distance in m 1*e-2
Quantum yield 0.61
Lifetime in ns 16
Extinction coef. 81000
Concentration 2*e-5
Thickness 1
● TCSPC
○ Time-gating
OW in ns 10
Time shift 0.05

Figure 4.11: The interface of the main window of the simulation tool.

While the simulator can be easily adjusted for any memory size, we recommend running the simulator on a computer with at least 2 GB of RAM.

4.9 Summary

This chapter presented the simulation model for fluorescence measurement experiment. First, we explained our motivation for the choice of simulation modelling. Then we introduced the simulation model and described the details of the functionality of each of its parts. Finally, we briefly described the implementation of the model.

Chapter 5

Experimental evaluation

5.1 TCSPC and time-gating under measurement of fluorescence with short and long lifetimes

To validate the system's capabilities to model different measurement techniques, we simulated the fluorescence decay measurements described in [15]. CdSe/ZnS quantum dots in toluene [71] in a glass capillary were put in the immediate proximity to the detector. A Picoquant LDH-P-C-470 [68] pulsed diode laser with 80 ps FWHM and 1 MHz repetition frequency was used as the excitation source. The practical and simulated laser pulses are shown in Figure 5.1 (the simulated graph has been obtained from the histogram of simulated photons, scaled to the peak of the measured graph). As one can see, the modelled laser shape does not have a long tail and thus it is a little bit narrower under the same FWHM.

Neither lenses nor optical filters have been used. A single CMOS SPAD pixel was employed to detect the fluorescence. The detector uses active quenching and has the characteristics described in Table 5.1

A theoretical lifetime of 16 ns has been utilized to simulate fluorescence decay. A 10-ns observation window and 60-ps time step were used for time-gating. The experimental and simulated fluorescence decay curves

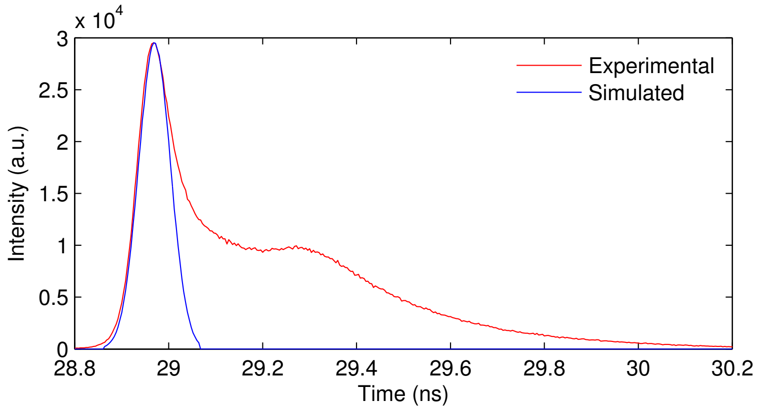

Figure 5.1: Simulated and practical laser pulse.

Table 5.1: The main characteristics of the SPAD in the measurement setup.

Dark count rate	4 kHz
Afterpulsing probability	∼ 4.5%
PDP	max 32% at 450 nm
Dead time	520 ns
FWHM of time response	160 ps

are shown in Figure 5.2. The difference of the intensity in the experimental and simulated data during the first 10 ns can be explained by non-metering of light dispersion in the fluorescent sample. All the unabsorbed photons hit the detector, whereas in the real world a proportion of them are lost. The lifetime for each curve has been estimated by means of fitting the fluorescence decay with a mono-exponential curve. The experimental and simulated lifetimes are 16.21 ns and 16.39 ns respectively.

Simulation of the fluorescence lifetime detection by time correlated single photon counting technique is presented in Figure 5.3. The result has been compared with the experimental data obtained with the same setup as in the previous case, except that we used an external commercial TCSPC instrument PicoHarp 300 [68].

As the parameters influencing the number of photons (such as beam divergence, geometry of setup, etc.) were not considered within this simu-

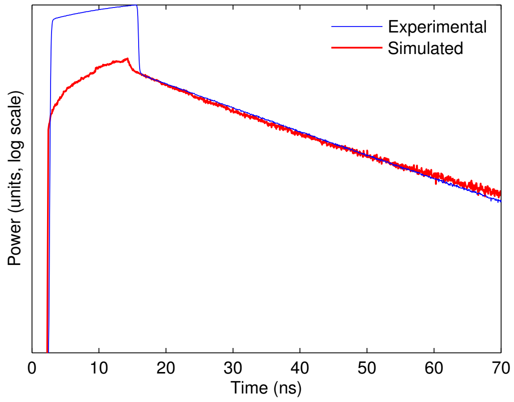

Figure 5.2: Fluorescence decay measurement performed with single pixel SPAD CMOS sensor and time-gated technique and simulated by our system.

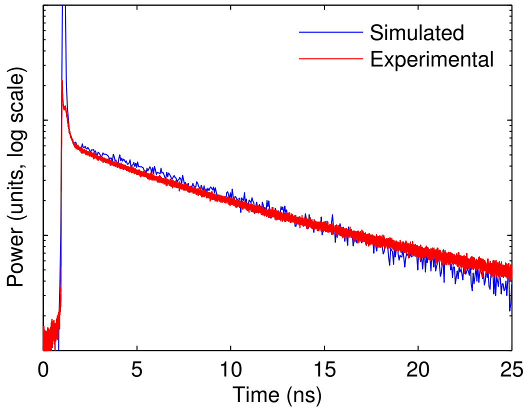

Figure 5.3: Fluorescence decay measurement performed with single pixel of SPAD CMOS sensor and TCSPC module and simulated by our system.

lation, only the shape of the simulated curves was verified. The simulated graphs were obtained from the histograms of simulated photons, scaled to the peak of the fluorescence part of the measured graphs. The quality of the simulation in both cases was checked by the chi-square test [70]. It indicated a good agreement between simulated and measured data.

5.2 A two-chip micro-system structure of micro-LED and SPAD detector

In this section we perform and evaluate the modelling of a two-chip "sandwich" structure (see Figure 5.4) which includes

- a blue micro-LED array with peak emission wavelength of 450 nm,
- a CMOS SPAD detector array where each pixel can extract time-gated measurements or send data to external photon counting hardware [72].

For this experiment a single pixel in the SPAD array and the nearest LED from the LED array were selected. The sample (CdSe/ZnS quantum dots in toluene [71]) in a micro-cavity slide and an excitation filter (Semrock, LP02-514RU-25 [73]) were placed into the 14 mm gap between the excitation and detection planes. A time-correlated single photon counting module (Becker and Hickl, SPC-130 [74]) was used to build the fluorescence decay curves.

A range of experiments with different light pulse width has been carried out to evaluate the sensitivity of the simulator. The backward simulation type has been used. The losses due to LED beam divergence, nonradiation absorption, finite detection area and filtering have been calculated based on Table 4.2. The full list of the setup characteristics is presented in Appendix A.1. Figure 5.5 presents the simulated and the experimental results for 3.1 ns, 3.15 ns and 3.3 ns pulse width with 3.77 μW, 6.47 μW

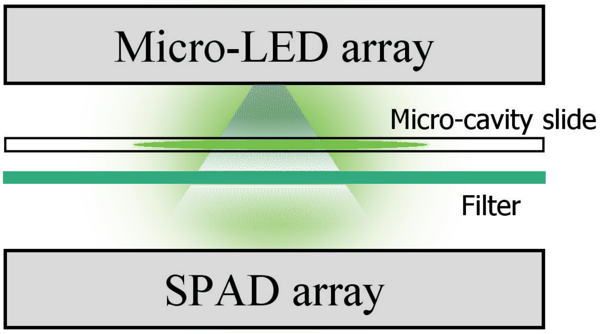

Figure 5.4: A two-chip "sandwich" structure including a micro-LED array and a CMOS SPAD detector array. The fluorescent sample was located in a micro-cavity slide. An excitation filter was used to separate the LED light from the fluorescent light.

and 9.08 μW average optical power, respectively. The simulated curves are in good agreement with the experimental ones.

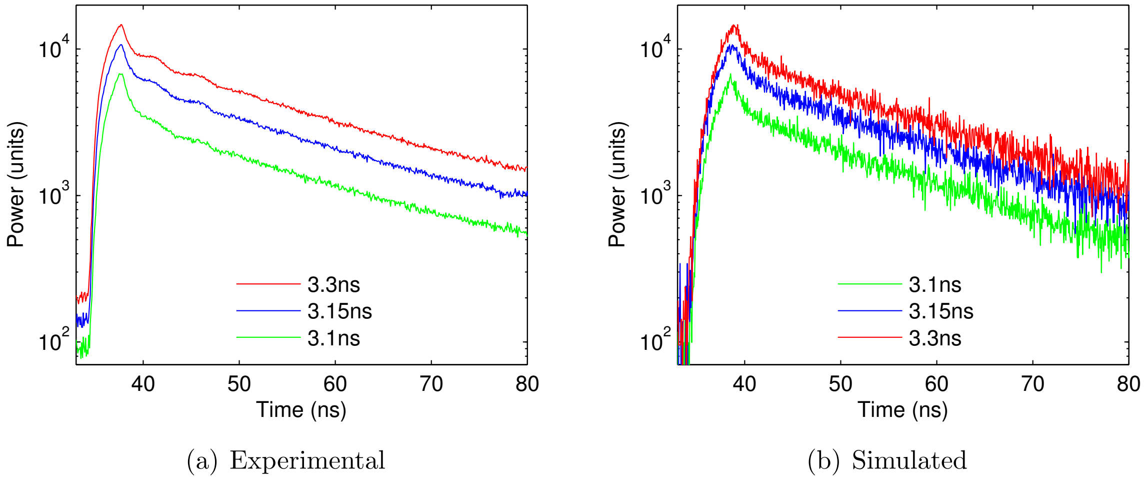

(a) Experimental

(b) Simulated

Figure 5.5: Experimental and simulated fluorescence decays with different light pulse width.

Another set of experiments has been performed to estimate the quantitative simulation ability of the model. We investigated different setups, with and without excitation filter and fluorescent sample. Selected results are presented in Figure 5.6. In those experiments, the dark count rate had been artificially increased to simulate the ambient light. The experimental

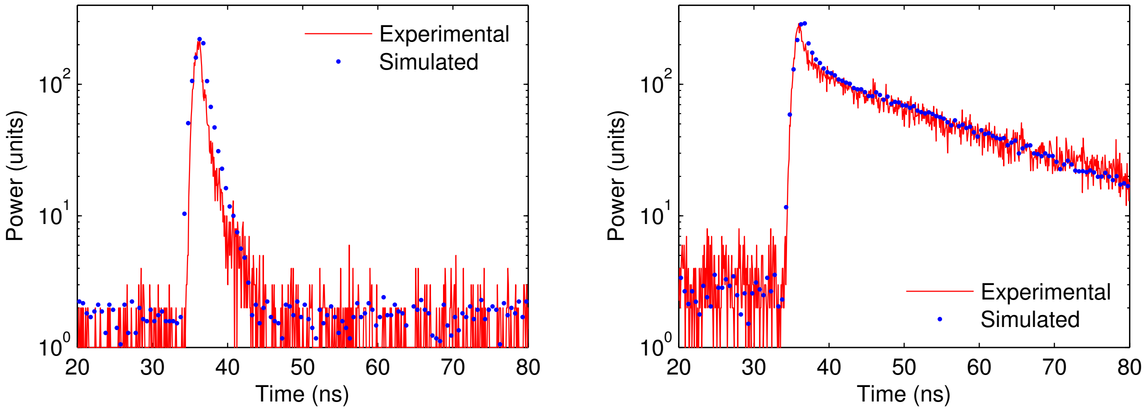

(a)

(b)

Figure 5.6: a) Experimental and simulated curves measured without fluorescence sample; b) experimental and simulated fluorescence decay.

and simulated data are in good agreement, except the peak area. This mismatch can be explained by inaccuracy of input parameters. Indeed, we did not have the experimental LED time curve at FWHM=2 ns. The time curve shape for with FWHM=2.2 ns has been squeezed to proper width. The distortion of the curve shape has probably resulted in the disagreement described above.

5.3 Investigation of pile-up effect under high light intensity conditions

In this experiment, we applied the simulation model to explain the distortions in experimental fluorescence decay measured under conditions that cause pile-up effect.

CdSe/ZnS quantum dots in toluene evidot® 620 [71] in a micro cavity were put in the immediate proximity to a commercial SPAD from Micro Photon Devices PDM series [75]. The fluorescence decay was rebuild by an external TCSPC module PicoHarp 300 [68]. A Picoquant LDH-P-

C-470 [68] pulsed diode laser with 80 ps FWHM and 1 MHz repetition frequency was used as excitation source. Due to the fact that no optical filter was used and the laser was directed straight into the detector, the SPAD worked in a saturated mode. The experimental curves are presented in Figure 5.7.

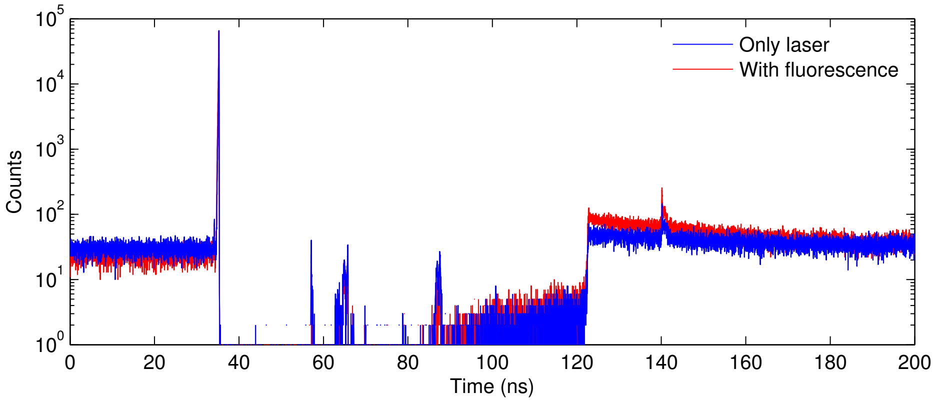

Figure 5.7: The experimental curves measured under pile-up effect.

To simplify the analysis, the curve without fluorescence emission was considered at the beginning.

The gap after the laser peak can be explained by the presence of dead time of TCSPC module, which worked in a multi-photon operation mode. The data sheet value of PicoHarp 300 is <95 ns, the one extracted from measurements is 85.5 ns.

To explain such artefacts as the increasing number of counts near the end of TCSPC dead time and the decay with long time constant after this time, we performed a range of simulations of this system with different levels of ambient light. Selected results are presented in Figure 5.8. These results correspond to the observed ones, part of which is presented in Figure 5.7.

The first artefact (counts within TCSPC dead time) can be explained by the following. Ideally, the laser photon detected at 35 ns triggers the avalanche and the system cannot detect other photons for the next 85.5 ns

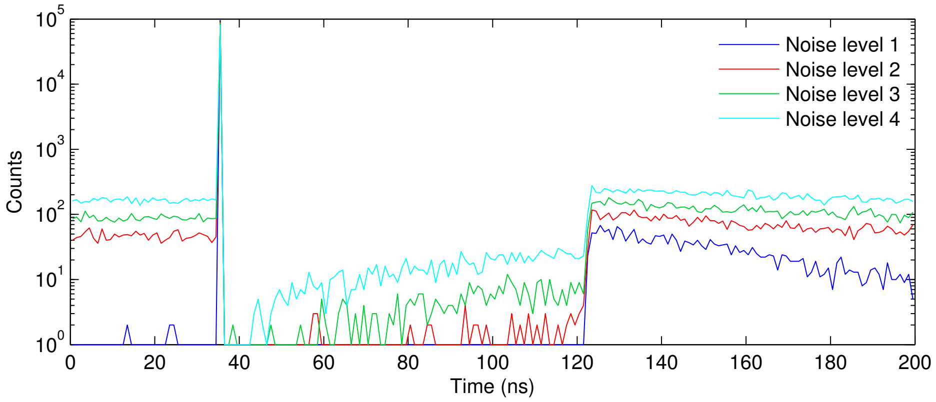

Figure 5.8: Simulation of laser light with different level of ambient noise. (Noise level 1 < Noise level 2 < Noise level 3 < Noise level 4)

(i.e., the dead time period). However, there is a chance that the SPAD detects a noise photon before the laser pulse. As the noise level increases, so do the chances of such detection. A noise photon detected at, for example, 20 ns will create a dead time period until 105.5 ns, so the system will be able to detect new photons before the end of the dead-time period caused by a laser peak (120.5 ns). This explains the photon counts within the dead-time gap of the system.

The second artefact is the shape of the curve after the TCSPC dead time and its slightly higher level that that before the laser peak. This artefact is caused by afterpulsing.

The next step was to explain the weak peaks over the whole detection period. As soon as the simulation did not show any similar peaks, we supposed that they are caused by imperfect adjustment of the experimental setup. After several attempts, it was found that these peaks are caused by noise pickups in the synchronization cable. The Figure 5.9 shows our best attempt to minimise this influence.

Finally, we included the fluorescence into the modelling, in order to simulate the curve of interest completely. The results are presented in Figure 5.10.

This section has demonstrated the ability of the proposed simulation model to help in explanation of some unexpected results of real measurements.

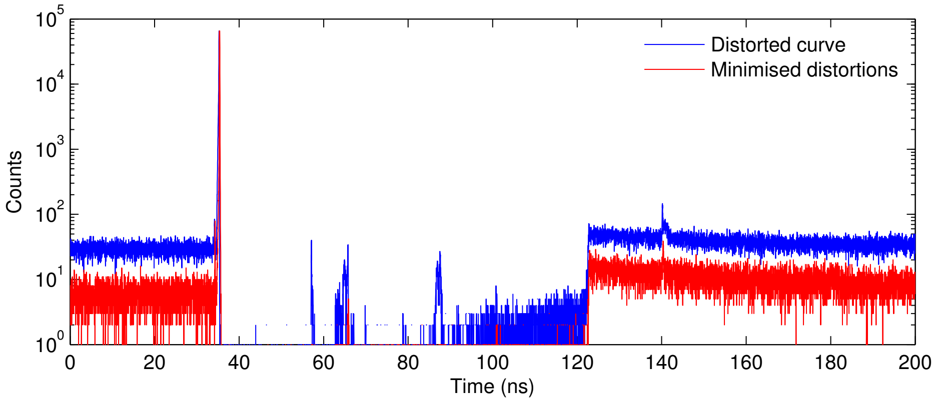

Figure 5.9: The best attempt to minimise the noise pickups in synchronization cable.

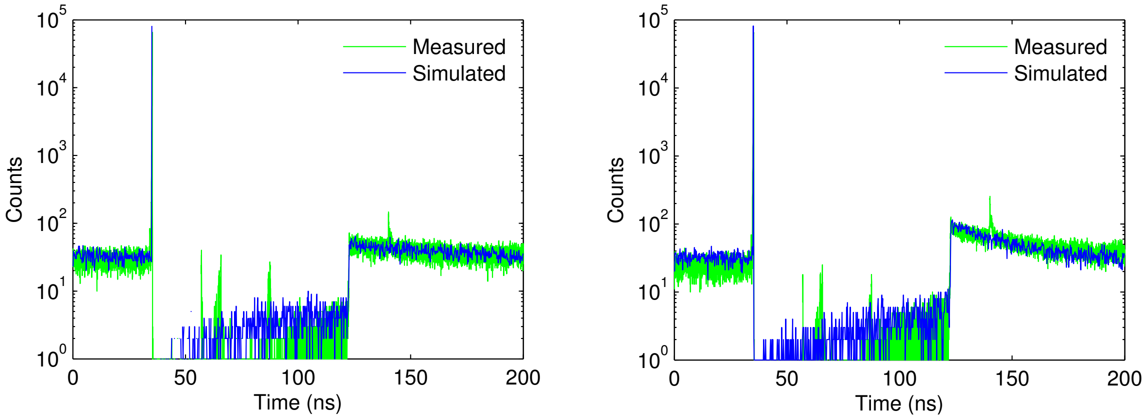

(a) Laser light (b) Fluorescence decay

Figure 5.10: Simulated and measured laser light and fluorescence decay curves under high ambient light level.

5.4 Investigation of time-filtering and noise effect in a microarray system

5.4.1 The system overview and research questions

The system considered in this experiment consists of a SPAD-based detector array and micro-cavities module. The schematic diagram of the system is presented in Figure 5.11. The SPAD array has been manufactured by a high voltage 0.35 μm CMOS technology (a similar detector has been reported in [13]). The array contains 10×10 pixels, and the active area of each pixel equals to 18.1×18.1 μm. The micro-cavity module is aligned with the SPAD array such that the centre of cavity is situated directly above the centre of the single pixel. The cavities have a diameter of 50 μm. The distance between the fluorescent and the detecting surfaces is 100 μm.

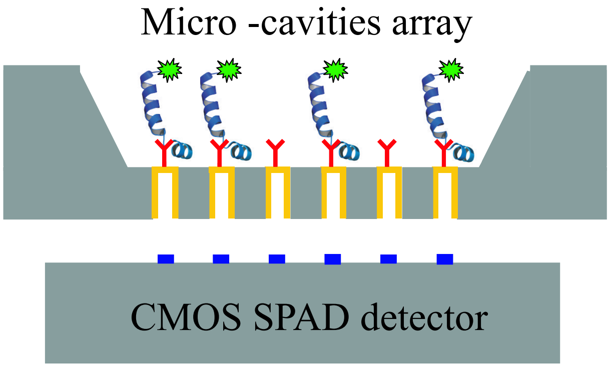

Figure 5.11: The schematic view of the system. CMOS SPAD detector and micro-cavities array with attached fluorophores are displayed. The figure is adapted from [76].

The SPAD array has an average DCR of 900 Hz for 80% of pixels and up to 150 kHz for the rest of the array (see Figure 5.12). The time-gating technique has been used to detect the fluorescence. Two consecutive gates with the width adjustable in the range of 0.8 ns – 10 ns were implemented.

The SPAD uses active quenching with the recharging time in the range

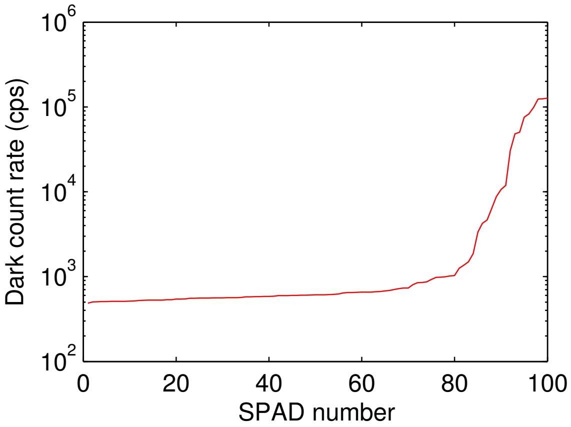

Figure 5.12: Dark count rates of single pixels, sorted in ascending order.

of nanoseconds. This time depends on total capacitance C_t which is the sum of the input capacitance of comparator C_c, the SPAD stray capacitance C_s and the capacitance of the Mn transistor C_n (see Figure 5.13). At the same time, C_n depends on the Mn transistor width w. Therefore, the total capacitance also has a dependence on w and is represented as $C_t(w)$. The recharging time has been simulated in PSpice for three different transistor widths w and $C_c + C_s$ equal to 100 fF. The results are presented in Table 5.2. It should be noted that for this range of w, the influence of C_n on total capacitance is negligible in comparison to $C_c + C_s$.

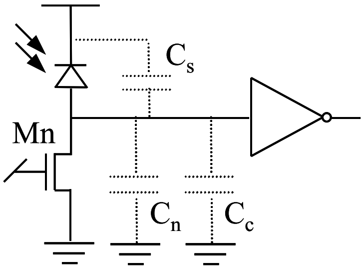

Figure 5.13: A simplified SPAD diagram.

The light source was simulated as a PicoQuant pulsed diode laser LDH-D-C-470 [68], and the simulated fluorophore was the Alexa Fluor® 488 [77]. The full list of the setup characteristics is presented in Appendix A.2.

Table 5.2: The PSpice simulation of the recharging time.

w	**time**
0.75 μm	1.76 ns
1.5 μm	0.8 ns
3 μm	0.4 ns

In this experiment we investigated the following questions:

1. How perfect is the time-filter in comparison to the conventional optical filter?
2. What is the influence of the “noisy” pixels on the lifetime estimation?
3. How does the OW width affect the lifetime estimation?

5.4.2 Simulation of time-filtering

The fluorescence was detected by time-gating with two consecutive gates. The rising and falling edges of the gates are not exactly vertical, because the rising/falling time is finite. The experimentally measured observation windows and the approximation used in the simulation are presented in Figure 5.14. The experimental data were taken for the last two 6 and 10 ns OWs of the detector presented in [13]. The estimated rising and falling time is 0.8 ns. This value was used for the simulation of photon counting at the rising edge. More specifically, the probability to count a photon increases linearly from 0 to 1 on the time interval $[startOW; startOW + 0.8\ ns]$. The falling edge was simulated similarly.

The PicoQuant laser pulse with FWHM=80 ps was simulated as a Gaussian with the mean value of 150 ps and σ value of 36 ps (4.11) . Such an approximation is valid for low power levels of the diode, when the laser does not have broadening caused by shoulder and/or additional peaks [68]. The laser light fades over 0.3 ns. So, to do the time-filtering the SPAD

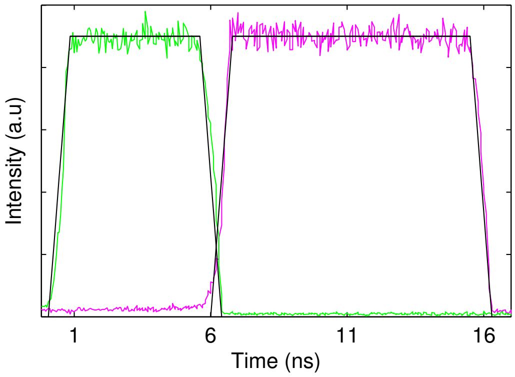

Figure 5.14: The measured and approximated observation windows.

should be switched off until this time. The simulation of the fluorescence detection with 6 and 10 ns OWs and 0.3 ns of time-filtering is presented in Figure 5.15. It is possible to observe the fluorescence decay even in the case of time-filtering. The delay of 0.5 ns between laser falling edge and OW rising edge corresponds to the SPAD recharging process. The lifetime extracted using equation (2.6) was 3.96 ns.

Figure 5.16 illustrates the simulation of fluorescence decay with the same width of time gates, but a smaller SPAD switched off time (0.25 ns). Presence of the excitation light in the first time gate is obvious. In this case, the lifetime estimation was distorted to a smaller extent (2.8 ns) in comparison to the previous case.

5.4.3 Analysis of influence of the “noisy” pixels and OW width on the lifetime estimation

Separate pixels of the SPAD array have different DCR (see Figure 5.12). A range of experiments have been performed to study the influence of the noisy pixels othe n lifetime estimation across the whole chip. We simulated the fluorescence detection by 100 single SPADs with different DCR value in accordance with the curve depicted in Figure 5.12. Two equal time gates

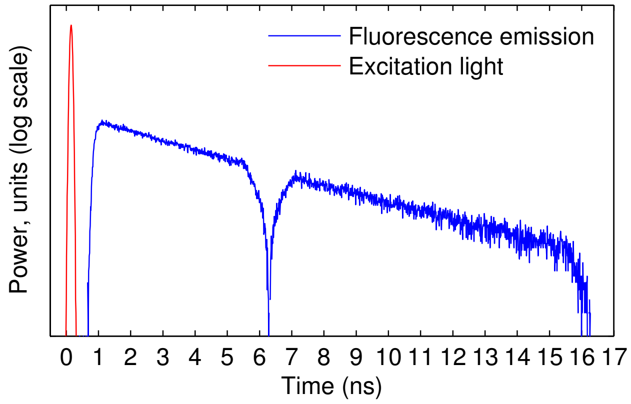

Figure 5.15: Time filtering simulation with 0.3 ns SPAD switched off time.

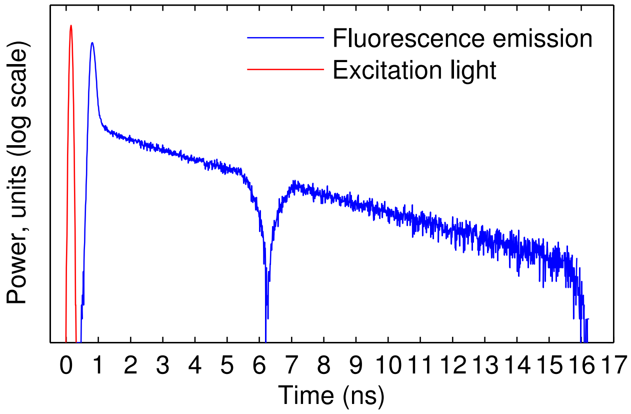

Figure 5.16: Time filtering simulation with 0.25 ns SPAD switched off time.

were used, so the lifetime extraction for each single SPAD was calculated by (2.6). Then the cumulative lifetime was calculated as follows:

$$\tau_i = \frac{T_1 - T_2}{\ln\left(\sum_{k=1}^{i} V_2^k / \sum_{k=1}^{i} V_1^k\right)}, \tag{5.1}$$

where $T_1 - T_2$ is the time distance between two time gates, $\sum_{k=1}^{i} V_2^k$ is the integrated intensity (i.e. number of counts) on the second time gate of the i^{th} SPAD and all $i-1$ previously simulated SPADs which have lower DCR.

The results of the simulation for 10 ns and 6 ns gate width are presented in Figure 5.17 and 5.18, respectively. It can be seen that for low-noise

SPADs the cumulative lifetime is a mean value of the lifetime per single pixel. In other words, the averaging over several SPADs with approximately equal DCR values decreases the statistical straggling of the lifetime estimation. On the other hand, the SPADs with a high DCR level should better be excluded from consideration. The exact number of SPADs, which should be involved into the lifetime estimation to achieve the best possible precision, can be found by repeating this simulation many times and performing a statistical analysis of the results.

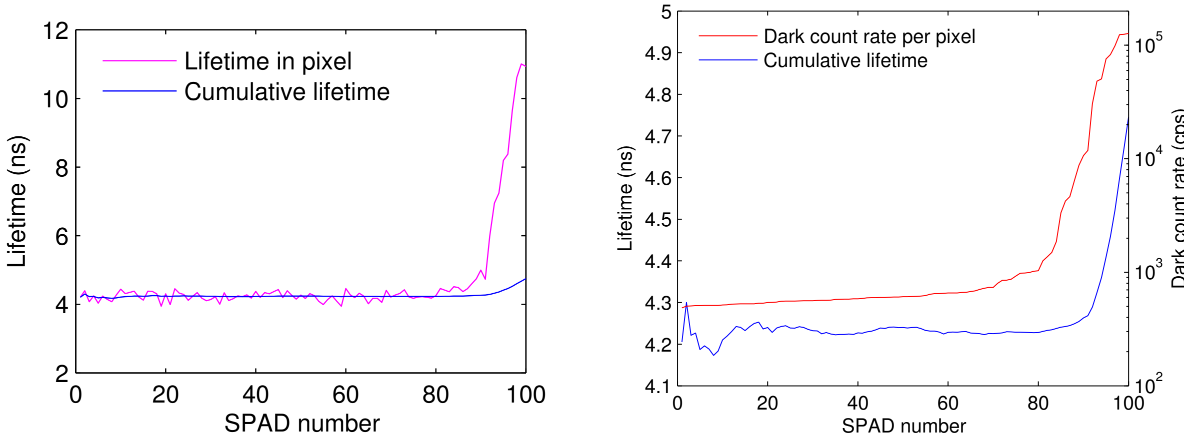

(a) Estimation of the lifetime per single pixel and cumulative lifetime

(b) Cumulative lifetime estimation and DCR value

Figure 5.17: Lifetime estimation for 100 separate pixels which have different DCR value. The widths of the time gates were 10 ns.

Some interesting results were obtained in the case of 6 ns time gates. Such a gate width is not perfect for the measurement of 4.1 ns lifetime [10]. The averaging over several SPADs with approximately equal DCR values in this case improves not only the precision but also the accuracy of the lifetime estimation.

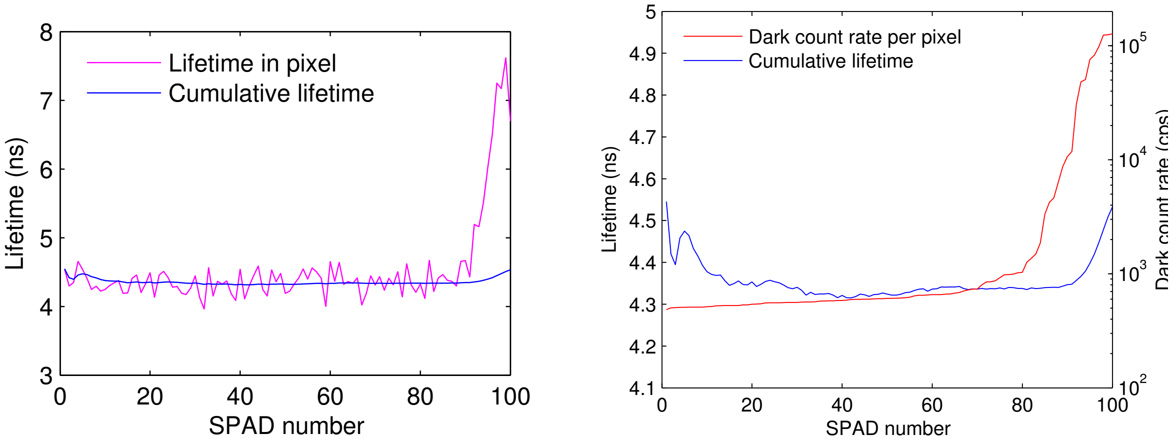

(a) Estimation of the lifetime per single pixel and cumulative lifetime

(b) Cumulative lifetime estimation and DCR value

Figure 5.18: Lifetime estimation for 100 separate pixels which have different DCR value. The widths of the time gates were 6 ns.

5.4.4 Discussion

The simulation has demonstrated the good performance of the time-filtering in SPAD detector. We found that by switching off the SPAD for a half of nanosecond it is possible to completely remove the laser light from detection. At the same time, it does not influence the lifetime extraction, because fluorescence emission takes at least one order of magnitude longer time than the SPAD switching-off time.

The time-filtering has several advantages in comparison to the conventional optical filter. First of all, if the time-filtering is used, the excitation wavelength can be selected at the peak of absorption spectrum even for the fluorophores with small Stokes shift. In the case of a very weak fluorescence signal, the optical filter (which has high but not 100% cutoff and transmission efficiency) will not be able to satisfactorily reduce the excitation signal without significant attenuation of the fluorescence signal.

To find a trade-off between time- and optical-filtering, additional research is required. In the described above case, the quantitative simulation was impossible due to the absence of knowledge about physicochemical processes inside the system of a single layer of complex molecules labeled by fluorophores. In such a system, numerous effects can change the intensity and the lifetime of the fluorescence.

The simulation of SPAD array with different noise level across the pixels has demonstrated that the averaging over several single SPADs with small DCR values improves precision of the lifetime estimation, whereas the SPADs with a high DCR level should be excluded from the consideration. Additional statistical analysis is necessary to find the exact number of single SPADs which should be involved into the lifetime estimation.

Finally, the simulation of lifetime extraction with different OW widths has shown that, in the case of non-optimal gate width, averaging over several single SPADs with small DCR values improves not only the precision but also the accuracy of the lifetime estimation. This can be useful when limited OW widths are used for long lifetime fluorescence decay.

Chapter 6

Conclusions

6.1 Summary

To find the optimal performance of single photon avalanche diodes in a specific application area, it is crucial to consider in a systematic manner both the detector characteristics and the experimental conditions. The area of research interest of this project was in the application of SPAD-based detectors in time-resolved fluorescence measurements. In this thesis, we proposed a simulation model of a typical experimental setup for fluorescence decay measurement. The model considers all the essential parts of this type of experiments, such as: the excitation light source, the fluorescent sample, the detector – as well as the measurement technique.

The experimental validation of the model demonstrated a very good qualitative matching to the real experimental results. The quantitative simulation, however, rather pretty accurate, is more prone to errors due to the following reasons. Firstly, the simulation modelling is very sensitive to the input parameters which should be as close as possible to the real world values. Even minor inaccuracies in the values of some parameters can lead to considerable large quantitative errors. The second source of the simulation error stems from the assumptions accepted for the simulation. In some of the real world experiments these assumptions might not hold, thus leading to simulation errors. In spite of this, the proposed model has been successfully applied to explain the distortions in experimental fluorescence decay measured under high intensity of ambient light, when the pile-up effect appears. Moreover, the prediction ability of the model has enabled the simulation-based investigation of the time-filtering and influence of noisy pixel in SPAD array on accuracy of lifetime estimation.

6.2 Future work

This project can be extended in several ways. First of all, the development of more advanced models of the experiment components will improve the accuracy of the simulation. For example, for a miniaturized system the consideration of the fluorescent sample as a point light source is not applicable. Future work may consider the inclusion of an appropriate correction coefficient or even take a different approach of fluorescence emission simulation. Secondly, the consideration of more complex biological samples will increase the application area. For instance, the simulation of energy transfer inside a fluorescent solution would enable the modelling of FRET systems. Also, the implementation of an optimization algorithm will provide an opportunity to fit SPAD and experimental setup parameters to achieve the optimal system performance. Finally, the system performance can be improved by conversion of the MATLAB model to some compiled programming language.

6.3 Conclusion

The project has demonstrated the utility of investigation of fluorescence measurements with SPAD-based detectors at the system level. Taking into account the conditions of the experimental setup, the measurement technique and the knowledge about all SPAD characteristics allows the researchers not only to reproduce the experimental data but also to predict results of real or planned experiments and thus optimize the implementation efforts.

The proposed methodology enables the preproduction-stage investigation of the importance of particular characteristics of the detectors for a particular application area. This makes it possible to design a SPAD with the optimal performance for the specific application.

Appendix A

Appendices

A.1 Characteristics of two-chip micro-system

Table A.1: The light source characteristics.

Characteristic	**Real value**	**Simulated value**	**Notes**
Time characteristic	FWHM=3.1/3.15/ 3.3 ns	FWHM=3.1/3.15/ 3.3 ns	Tabulated curves from an experiment
Spectrum	450 ($\pm$30)nm	450 ($\pm$30)nm	Tabulated curve from an experiment
Power per pulse	3.77/6.47/9.08 μW	3.77/6.47/9.08 μW	
Beam shape	Circle with diameter 20 μm	Circle with diameter 20 μm	Data from [78]
Divergence	75°	75°	Data from [78]

Table A.2: The SPAD characteristics.

Characteristic	**Real value**	**Simulated value**	**Notes**
Dead time	30 - 40 ns	30 - 40 ns	Passive quenching simulation
SPAD active area	$\varnothing 6\ \mu m$	$\varnothing 6\ \mu m$	
DCR	30 Hz	30 Hz	
PDP	35% max at 460 nm	35% max at 460 nm	Tabulated curve from experiment
Afterpulsing probability	—	0.249%	

Table A.3: The fluorophore characteristics.

Characteristic	**Real value**	**Simulated value**	**Notes**
Concentration	81.33 M	81.33 M	
Thickness	0.5 mm	0.5 mm	
Quantum yield	0.61	0.61	
Extinction coefficient	81000	81000	
Lifetime	20 ns	20 ns	
Spectra	Emission peak 526 nm	Emission peak 526 nm	

Table A.4: Geometry of the setup.

Characteristic	**Real value**	**Simulated value**	**Notes**
LED - fluorophore distance	≈ 5 mm	6 mm	
Fluorophore - SPAD distance	≈ 9 mm	9 mm	
Filter probability	≈ 98%	98%	

A.2 Characteristics of microarray system

Table A.5: The light source characteristics.

Characteristic	**Real value**	**Simulated value**	**Notes**
Time characteristic	FWHM=80 ps	FWHM=80 ps	Gaussian with mean=0.15 ns and 0.0361 ns [1]
Spectrum	470 (±10)nm	Peak 470 FWHM=20 nm	Gaussian with mean=470 ns and 8.4932 ns
Power per pulse	0.3 mW	0.3 mW	
Beam shape	Circle with diameter 3.5 mm	Circle with diameter 3.5 mm	In case of using a multi mode optical fibre [68]

Table A.6: The fluorophore characteristics.

Characteristic	**Real value**	**Simulated value**	**Notes**
Concentration	10^{11} molecules/cm^2	10^{11} molecules/cm^2	Single layer
Optical cross-section	$1.23*10^{-20}$ m^{-2}	$1.23*10^{-20}$ m^{-2}	
Quantum yield	0.92	0.92	
Lifetime	4.1 ns	4.1 ns	
Spectra	Excitation peak 499 nm, emission peak 519 nm	Excitation peak 499 nm, emission peak 519 nm	Tabulated curve from the site of producer of Alexa Fluor® 488 [77]

---

[1] This approximation of laser shape valid for PicoQuant laser with low power level [68].

Table A.7: The SPAD characteristics.

Characteristic	**Real value**	**Simulated value**	**Notes**
Dead time	$150ns$–10 μs	$150ns$	
SPAD active area	18.1×18.1 μm	18.1×18.1 μm	
DCR	900 Hz–100 kHz	900 Hz–100 kHz see Figure 5.12	For simulation of single pixel 900 Hz value was used
Recharge time	0.4–1.76 ns	0.4, 0.8, 1.76 ns	
Comparator threshold	1.5 V	1.5 V	
PDP	33% max at 450 nm	33% max at 450 nm	Tabulated curve from [15] for $V_e = 4$V
Afterpulsing probability	8.2% for DCR=900 Hz and dead time 150 ns	8.2%	Tabulated curve from [15]
Time response	FWHM=160 ps	FWHM=160 ps	Tabulated curve from [15]
Time-gating	Two consecutive OWs from 0.8–10 ns	3&10 ns, 6&6 ns, 6&10 ns, 10&10 ns	The beginning of the first OW was different depending on time-filtering

Bibliography

[1] V. D. Rumyantseva, G. M. Sukhin, I. P. Shilov, V. M. Markushev, A. F. Mironov, and A. V. Ivanov. Laser infra-red luminescence diagnostics of tumours with use of ytterbium-complexes of porphyrin. *Photodiagnosis and Photodynamic Therapy*, 5(1):S27, 2008.

[2] X. Xiong, D. Xiao, and M. M. F. Choi. Dissolved oxygen sensor based on fluorescence quenching of oxygen-sensitive ruthenium complex immobilized on silicanip composite coating. *Sensors and Actuators B: Chemical*, 117(1):172–176, 2009.

[3] P.V. Nazarov, R.B.M. Koehorst, W.L. Vos, V.V. Apanasovich, and M.A. Hemminga. Fret study of membrane proteins: determination of the tilt and orientation of the n-terminal domain of M13 major coat protein. *Biophysical journal*, 92(4):1296–1305, 2007.

[4] R. W. Wood. The time interval between absorption and emission of light in fluorescence. *Proceedings of Royal Society A*, 99:362–371, 1921.

[5] R. G. Bennet. Instrument to measure fluorescence lifetimes in the millimicrosecond region. *Review of Scientific Instruments*, 31(12):1275–1279, 1960.

[6] G. G. Guilbault. *Practical Fluorescence.* Marcel Dekker, Inc., 1990.

[7] J. R. Lakowicz. *Principles of fluorescence spectroscopy.* Springer, 3rd edition, 2006.

[8] B. Valeur. *Molecular Fluorescence: Principles and Applications.* Wiley-VCH, 2001.

[9] E. B. van Munster and T. W. J. Gadella. Fluorescence lifetime imaging microscopy (FLIM). *Advances in Biochemical Engineering/Biotechnology*, 95:143–175, 2005.

[10] H. C. Gerritsen, M. A. H. Asselbergs, A. V. Agronskaia, and W. G. J. H. M. van Sark. Fluorescence lifetime imaging in scanning microscopes: acquisition speed, photon economy and lifetime resolution. *Journal of Microscopy*, 206(3):218–224, 2002.

[11] H. J. Yoon and S. Kawahito. A CMOS image sensor for fluorescence lifetime imaging. In *Proceedings of 5th IEEE Conference on Sensors*, pages 400–403, 2006.

[12] D. Mosconi, D. Stoppa, L. Pancheri, L. Gonzo, and A. Simoni. CMOS single-photon avalanche diode array for time-resolved fluorescence detection. In *Proceedings of ESSCIRC*, pages 564–567, 2006.

[13] L. Pancheri and D. Stoppa. A spad-based pixel linear array for high-speed time-gated fluorescence lifetime imaging. In *Proceedings of ESSCIRC'09*, pages 428 – 431, 2009.

[14] B. R. Rae, C. Grifn, K. R. Muir, J. M. Girkin, E. Gu, D. Renshaw, E. Charbon, M. D. Dawson, and R. K. Henderson. A microsystem for time-resolved uorescence analysis using cmos single-photon avalanche diodes and micro-leds. In *Proceedings of IEEE ISSCC*, pages 166–603, 2008.

[15] D. Stoppa, D. Mosconi, L. Pancheri, and L. Gonzo. Single-photon avalanche diode cmos sensor for time-resolved fluorescence measure-

ments. *IEEE Sensors Journal*, 9(9):1084–1090, 2009. doi: 10.1109/JSEN.2009.2025581.

[16] S. Cova, A. Longoni, and A. Andreoni. Toward picosecond resolution with single-photon avalanche diodes. *Review of Scientific Instruments*, 52(3):408–412, 1981.

[17] R. H. Haitz. Model for the electrical behavior of a microplasma. *Journal of Applied Physics*, 35(5):1370 – 1376, 1964.

[18] R. H. Haitz. Mechanisms contributing to the noise pulse rate of avalanche diodes. *Journal of Applied Physics*, 36(10):3123 – 3131, 1965.

[19] A. Gulinatti, I. Rech, P. Maccagnani, M. Ghioni, and S. Cova. Large-area avalanche diodes for picosecond time-correlated photon counting. In *Proceedings of 35th European Solid-State Device Research Conference (ESSDERC)*, pages 355–358, 2005.

[20] A. Spinelli, M. A. Ghioni, S. D. Cova, and L. M. Davis. Avalanche detector with ultraclean response for time-resolved photon counting. *IEEE Journal of Quantum Electronics*, 34(5):817–821, 1998.

[21] A. Lacaita, S. Cova, M. Ghioni, and F. Zappa. Single-photon avalanche diodes with ultrafast pulse response free from slow tails. *IEEE Electron Device Letters*, 14(7):360–362, 1993.

[22] S. Cova, M. Ghioni, A. Lotito, I. Rech, and F. Zappa. Evolution and prospects for single-photon avalanche diodes and quenching circuits. *Journal of Modern Optics*, 51(9–10):1267–1288, 2004.

[23] M. Ghioni, A. Gulinatti, I. Rech, F. Zappa, and S. Cova. Progress in silicon single-photon avalanche diodes. *IEEE Journal of Selected Topics in Quantum Electronics*, 13(4):852 – 862, 2007.

[24] F. Zappa, S. Tisa, A. Tosi, and S. Cova. Principles and features of single-photon avalanche diode arrays. *Sensors and Actuators A: Physical*, 140(1):103–112, 2007.

[25] D. Cronin and A.P. Morrison. Intelligent system for optimal hold-off time selection in an active quench and reset IC. *IEEE Journal of Selected Topics in Quantum Electronics*, 13(4):911 – 918, 2007.

[26] S. Cova, M. G., A. Lacaita, C. Samori, and F. Zappa. Avalanche photodiodes and quenching circuits for single-photon detection. *Applied Optics*, 35(12):1956–1976, 1996.

[27] H. Finkelstein, M.J. Hsu, S. Zlatanovic, and S. Esener. Performance trade-offs in single-photon avalanche diode miniaturization. *Review of Scientific Instruments*, 78(10):103103–5, 2007.

[28] M.J. Hsu, H. Finkelstein, and S.C. Esener. A CMOS STI-bound single-photon avalanche diode with 27-ps timing resolution and a reduced diffusion tail. *IEEE Electron Device Letters*, 30(6):641–643, 2009.

[29] M. A. Itzler, R. Ben-Michael, C. F. Hsu, K. Slomkowski, A. Tosi, S. Cova, F. Zappa, and R. Ispasoiu. Single photon avalanche diodes (SPADs) for 1.5 um photon counting applications. *Journal of Modern Optics*, 54(2-3):283–304, 2007.

[30] J. A. Richardson, L. A. Grant, and R. K. Henderson. Low dark count single-photon avalanche diode structure compatible. *IEEE Photonics Technology Letters*, 21(14):1020 – 1022, 2009.

[31] Z. Xiao, D. Pantic, and R.S. Popovic. A new single photon avalanche diode in CMOS high-voltage technology. In *International Solid-State Sensors, Actuators and Microsystems Conference, TRANSDUCERS 2007*, pages 1365 – 1368, 2007.

[32] C. Niclass, C. Favi, T. Kluter, M. Gersbach, and E. Charbon. A 128x128 single-photon image sensor with column-level 10-bit time-to-digital converter array. *IEEEJournal of Solid-State Circuits*, 43(12): 2977–2989, 2008.

[33] C. Niclass, M. Gersbach, R. K. Henderson, L. Grant, and E. Charbon. A single photon avalanche diode implemented in 130nm cmos technology. *Journal of Selected Topics in Quantum Electronics*, 13(4): 863–869, 2007.

[34] M. Gersbach, Y. Maruyama, E. Labonne, J. Richardson, R. Walker, L. Grant, R. K. Henderson, F. Borghetti, D. Stoppa, and E. Charbon. A parallel 32x32 time-to-digital converter array fabricated in a 130 nm imaging CMOS technology. In *Proceedings of IEEE European Solid-State Device Conference (ESSCIRC)*, pages 196–199, 2009.

[35] A. Spinelli and A. L. Lacaita. Physics and numerical simulation of single photon avalanche diodes. *IEEE Transactions on Electron Devices*, 44(11):1931–1943, 1997.

[36] Li-Qiang Li and Lloyd M. Davis. Single photon avalanche diode for single molecule detection. *Review of Scientific Instruments*, 64(6): 15241529, 1993.

[37] T. Kagawa. Simulation of the geiger mode operation of a single photon detection avalanche photodiode. *IEICE Tansactions on Electronics*, E86-C(7):1366–1369, 2003.

[38] K. Sugihara, E. Yagyu, and Y. Tokuda. Numerical analysis of single photon detection avalanche photodiodes operated in the geiger mode. *Journal of Applied Physics*, 99(12):124502.1–124502.5, 2006.

[39] D. A. Ramirez and M. M. Hayat. Dependence of the performance of single photon avalanche diodes on the multiplication region width. *IEEE Journal of Quantum Electronics*, 44(12):1188–1195, 2008.

[40] Y. Kang, H. X. Lu, Y.-H. Lo, D. S. Bethune, and W. P. Risk. Dark count probability and quantum efficiency of avalanche photodiodes for single-photon detection. *Applied Physics Letters*, 83(14):2955–2957, 2003.

[41] J. C. Jackson, B. Lane, A. Mathewson, and A. P. Morrison. Simulation of dark count in geiger mode avalanche photodiodes. In *Proceedings of IEEE SISPAD2001*, pages 376–379, 2001.

[42] W. J. Kindt and H. W. van Zeijl. Modelling and fabrication of geiger mode avalanche photodiode. *IEEE Transactions on Nuclear Science*, 45(3):715–719, 1998.

[43] J. C. Jackson, D. Phelan, A. P. Morrison, R. M. Redfern, and A. Mathewson. Characterization of geiger mode avalanche photodiodes for fluorescence decay measurements. In *Proceedings of SPIE*, volume 4650, pages 55–66, 2002.

[44] J. C. Jackson, D. Phelan, A. P. Morrison, R. M. Redfern, and A. Mathewson. Toward integrated single photon counting microarrays. *Optical Engineering*, 42(1):112–118, 2003.

[45] I. Rech, A. Ingargiola, R. Spinelli, I. Labanca, S. Marangoni, M. Ghioni, and S. Cova. A new approach to optical crosstalk modeling in single-photon avalanche diodes. *IEEE Photonics Technology Letters*, 20(5):330–332, 2008.

[46] I. Rech, A. Ingargiola, R. Spinelli, I. Labanca, S. Marangoni, M. Ghioni, and S. Cova. Optical crosstalk in single photon avalanche

diode arrays: a new complete model. *Optics Express*, 16(12):8381–8394, 2008.

[47] M. Köllner and J. Wolfrum. How many photons are necessary for fluorescence-lifetime measurements? *Chemical Physics Letters*, 200 (1,2):199–204, 1992.

[48] D. V. O'Connor and D. Phillips. *Time-Correlated Single Photon Counting.* Academic Press: London, 1984.

[49] J. N. Demas. *Excited State Lifetime Measurements.* Academic Press: New York, 1983.

[50] H. C. Gerritsen, R. Sanders, A. Draaijer, and Y. K. Levine. The photon economy of fluorescence lifetime imaging. *Scanning*, 18(1): 57–58, 1996.

[51] C. J. de Grauw and H. C. Gerritsen. Multiple time-gate module for fluorescence lifetime imaging. *Applied Spectroscopy*, 55(6):670–678, 2001.

[52] K. Palo, U. Mets, V. Loorits, and P. Kask. Calculation of photon-count number distributions via master equations. *Biophysical journal*, 90(6):2179–2191, 2006.

[53] L.-Q. Li and L. M. Davis. Rapid and efficient detection of single chromophore molecules in aqueous solution. *Applied Optics*, 34(18): 3208–3217, 1995.

[54] D. H. Bunfield. Simulation of a single molecule detection experiment. Master's thesis, University of Tennessee, 1997.

[55] D.H. Bunfield and L.M. Davis. Monte carlo simulation of a single molecule detection experiment. *Applied Optics*, 37(12):2315–2326, 1998.

[56] Y. Sun, B. Whitehead, and L.M. Davis. Analysis of ultrasensitive fluorescence experiments. In *Proceedings of SPIE*, volume 3602, pages 379–390, 1999.

[57] L. M. Davis, J. G. K. Williams, and D. T. Lamb. Computer simulation of gene detection without PCR by single molecule detection. In *Proceedings of SPIE*, volume 3570, pages 282–293, 1999.

[58] T. Toni and M. P. H. Stumpf. Simulation-based model selection for dynamical systems in systems and population biology. *Bioinformatics*, 26(1):104–110, 2010.

[59] T. Halasa, M. Nielen, T. van Werven, and H. Hogeveen. A simulation model to calculate costs and benefits of dry period interventions in dairy cattle. *Journal of Livestock Science*, 129(1):80–87, 2010.

[60] T. Barker and S. S. Scrieciu. Modeling low climate stabilization with E3MG: Towards a new economics approach to simulating energy-environment-economy system dynamics. *The Energy Journal*, 31(1): 137–164, 2010.

[61] Z.-W. Li, Z.-Y. Sun, and Z.-Y. Lu. Simulation model for hierarchical self-assembly of soft disklike particles. *Journal of Physical Chemistry: B*, 14(7):23532358, 2010.

[62] G. Ullman, D. R. Dance, M. Sandborg, G. A. Carlsson, A. Svalkvist, and M. Bath. A monte carlo-dased model for simulation of digital chest tomosynthesis. *Radiation Protection Dosimetry*, 2010.

[63] K. M. Sage and E. A. Sykes. Evaluation of routing-related performance for large scale packet-switched networks with distributed, adaptive routing policies. *Information and decision technologies*, 19(6):543–562, 1994.

[64] E. W. Weisstein. Gaussian function. On-line: MathWorld–A Wolfram Web Resource. `http://mathworld.wolfram.com/GaussianFunction.html`. Accessed on 23 March 2010.

[65] W. H. Press, S. A. Teukolsky, W. T. Vetterling, and B. P. Flannery. *Numerical Recipes: The Art of Scientific Computing.* Cambridge University Press, 3rd edition, 2007.

[66] W. R. Leo. *Techniques for nuclear and particle physics experiments: a how-to approach.* Springer-Verlag, 2nd revised edition, 1994.

[67] C. W. Jeon, H. W. Choi, and M. D. Dawson. Fabrication of matrix-addressable InGaN-based microdisplays of high array density. *IEEE Photonics Technology Letters*, 15(11):1516 – 1518, 2003.

[68] PicoQuant GmbH. Ultraviolet to infrared picosecond diode laser heads. On-line: `http://www.picoquant.com/_products.htm`, . Accessed on 8 March 2010.

[69] Z. A. Karian and E. J. Dudewicz. *Modern Statistical, Systems, and GPSS Simulation.* CRC Press, 2nd edition, 1999.

[70] D. R. Anderson, D. J. Sweeney, and T. A. Williams. *Statistics for business and economics.* South-Western College Pub, 9th edition, 2005.

[71] Evident Technologies. Core and core-shell quantum dots. On-line: `http://www.evidenttech.com/products/evidots.html`. Accessed on 10 March 2010.

[72] Bruce R. Rae, Keith R. Muir, David Renshaw, Robert K. Henderson, John Girkin, Zheng Gong, Jonathan McKendry, Erdan Gu, and Martin D. Dawson. A vertically integrated CMOS micro-system for time-resolved fluorescence analysis. In *IEEE Biomedical Circuits and Systems Conference (BioCAS 2009)*, pages 85–88. IEEE, Nov 2009.

[73] Semrock. Lp02-514ru-25. On-line: `http://www.semrock.com/Catalog/Detail.aspx?CategoryID=69&FilterPartID=164`. Accessed on 10 March 2010.

[74] Becker & Hickl GmbH. Time-correlated single photon counting devices. On-line: `http://www.becker-hickl.com/tcspc.htm\#spc130`, . Accessed on 10 March 2010.

[75] Micro Photon Devices. MPD's single-photon detection modules. On-line: `http://www.microphotondevices.com/products_pdm.asp`. Accessed on 29 March 2010.

[76] E. Morganti, C. Collinin, L. Lorenzelli, F. Borghetti, D. Stoppa, and L. Gonzo. A multisite micro-reactor array for fluorescence-based bioaffinity assays. *Procedia Chemistry*, 1(1):1087–1090, 2009.

[77] Invitrogen. Alexa fluo® 488 dye. On-line: `http://www.invitrogen.com/etc/medialib/en/filelibrary/pdf/Brochures.Par.10443.File.dat/B-068179-AlexaFluor488_v2_HQP.pdf`. Accessed on 29 March 2010.

[78] C. Griffin, E. Gu, H. W. Choi, C. W. Jeon, J. M. Girkin, M. D. Dawson, and G. McConnell. Beam divergence measurements of ingan/gan micro-array light-emitting diodes using confocal microscopy. *Applied Physics Letters*, 86(4):041111:1–3, 2005. doi: 10.1063/1.1850599. LED .